1  **Effects of dynamic changes of desiccation cracks on preferential flow: Experimental investigation and**

2  **numerical modeling**

4  Yi Luo[1,2], Jiaming Zhang*[1], Zhi Zhou[3], Juan P. Aguilar-Lopez[4], Roberto Greco[5], Thom Bogaard[2]

5  [1] Faculty of Engineering, China University of Geosciences (Wuhan), Wuhan, 430074, China

6  [2] Water Resources Section, Faculty of Civil Engineering and Geosciences, Delft University of Technology, Stevinweg 1, P.O.
7    Box 5048, 2600 GA Delft, the Netherlands

8  [3.]Department of Engineering Management, Hubei University of Economics, Wuhan, 430205, China

9  [4.]Department of Hydraulic Engineering, Faculty of Civil Engineering and Geosciences, Delft University of Technology, Delft,
10   2600 GA, the Netherlands

11 [5.]Dipartimento di Ingegneria, Università degli Studi della Campania "Luigi Vanvitelli", via Roma 29, 81031, Aversa, Italy

12 *Correspondence to*: Jiaming Zhang (zjm@cug.edu.cn)

14 **Abstract:** Preferential flow induced by desiccation cracks (PF-DC) has been proven to be an important hydrological effect
15 that could cause various geotechnical engineering and ecological environment problems. Investigation on the PF-DC remains
16 a great challenge due to the soil shrinking-swelling behavior. This work presents an experimental and numerical study of the
17 PF-DC considering the dynamic changes of DC. A soil column test was conducted under wetting-drying cycles to investigate
18 the dynamic changes of DC and their hydrological response. The ratio between the crack area and soil matrix area (crack
19 ratio), crack aperture and depth were measured. The soil water content, matrix suction and water drainage were monitored. A
20 new dynamic dual-permeability preferential flow model (DPMDy) was developed, which includes physically-consistent
21 functions in describing the variation of both porosity and hydraulic conductivity in crack and matrix domains. Its performance
22 was compared to the single-domain model (SDM) and rigid dual-permeability model (DPM) with fixed crack ratio and
23 hydraulic conductivity. The experimental results showed that the maximum crack ratio and aperture decreased when the
24 evaporation intensity was excessively raised. The self-closure phenomenon of cracks and increased surficial water content
25 were observed during low evaporation periods. The simulation results showed that the matrix evaporation modeled by the
26 DPMDy is lower than that of the SDM and DPM, but its crack evaporation is the highest. Compared to the DPM, the DPMDy
27 simulated a faster pressure head building-up process in the crack domain and higher water exchange rates from the crack to
28 the matrix domain during rainfall. Using a fixed crack ratio in the DPM, whether it is the maximum or the average value from
29 the experiment data, will overestimate the infiltration fluxes of PF-DC but underestimate its contribution to the matrix domain.
30 In conclusion, the DPMDy better described the underlying physics involving crack evolution and hydrological response with
31 respect to the SDM and DPM. Further improvement of the DPMDy should focus on the hysteresis effect of the soil water
32 retention curve and soil deformation during wetting-drying cycles.

33 **Keywords:** Desiccation cracks; preferential flow; dynamic changes; dual-permeability model; wetting-drying cycles

34 **1. Introduction**

35 Desiccation cracks are prevalent in clay-dominated soils due to water loss, which often lead water to bypass the surface soil
36 matrix and rapidly infiltrate into subsoil as preferential flow (Davidson, 1984; Weiler, 2005). Positively, the preferential flow
37 induced by desiccation cracks (PF-DC) can promote the migration of farmland organic matter (Vervoort et al., 2003) and
38 reduce surface runoff (Pei et al., 2020; Zhang et al., 2021a). Negatively, it also has proven to be an important hydrological

39 mechanism that could lead to geotechnical engineering and ecological environment problems, such as dike and slope

40 instability (Jamalinia et al., 2020; Zhang et al., 2021b), shallow landslides (Bogaard and Greco, 2015; Caris and Van Asch,

41 1991; Luo et al., 2021), groundwater pollution (Chaduvula et al., 2022; Chen et al., 2002; Mooney and Morris, 2008; Schlögl

42 et al., 2022) and reduction of irrigation efficiency (Greve et al., 2010; Smith et al., 2005; Wang et al., 2018; Wang et al., 2022).

43 Under the current background of frequent extreme flood-drought climate events, its negative effects will be more prominent

44 (Tichavsky et al., 2019). Investigation on the PF-DC are of great significance in guiding scientific research and practical

45 design in the above disciplines.

46 A unique characteristic of the desiccation cracks is their dynamic features, often causing instantaneous variation of crack

47 proportion, depth and connectivity with moisture content. Previous efforts have attempted to reveal the effects of crack

48 dynamics on the PF-DC through experimental studies, but most of them focused on short-term wetting process and obtained

49 only qualitative results and debates remained. For instance, Favre et al. (1997)and Liu et al. (2003) stated that crack closure

50 due to wetting can cause a significant reduction or even disappearances in the preferential flow. However, other studies found

51 that the PF-DC also leads water to rapidly infiltrate into deep soil even when desiccation cracks are nearly closed (Baram et

52 al., 2012a; Greve et al., 2010; Luo et al., 2021; Tuong et al., 1996; Sander and Gerke, 2007). Cheng et al. (2021) conducted a

53 series of constant-head permeability tests with the hydraulic head gradient of 15 kPa. They stated that 4% of surface crack

54 ratio could be a critical value for determining whether desiccation cracks cause a significant increase in the infiltration rate or

55 not. However, this value may vary with different soils, rainfall patterns and sample scales, and thus lacks general applicability.

56 Indeed, PF-DC has long-term and complex spatiotemporal variability due to crack dynamics during wetting-drying cycles.

57 Therefore, short-term and small-scale infiltration tests (i.e. laboratory permeability tests) are not enough to reveal the complex

58 hydrological process induced by PF-DC. Meanwhile, it is also difficult to quantitatively study PF-DC only through

59 experiments. An improve understanding of the PF-DC combined with theoretical methods is also needed.

60 Regarding the theoretical methods, explicit crack models (EMs) (Hendrickx. and Flury, 2001; Khan et al., 2017; Xie et al.,

61 2020)), dual-porosity (DPoM) (Van Genuchten, 1980; Van Genuchten and Wierenga, 1976) and dual-permeability (DPM)

62 (Aguilar‐López et al., 2020; Gerke and Van Genuchten, 1993b, 1993a) models were developed to simulate preferential flow

63 in cracked clay soils. EMs were constructed based on the single-domain (or single-permeability) framework, which require

64 to define the details involving the geometry, spatial distribution and hydrological properties of each crack. Such requirement

65 may be conceptually correct but makes them difficult for simulating network-distributed desiccation cracks due to

66 considerable computational burden (Aguilar‐López et al., 2020). The DPoM and DPM concepts belong to the dual-domain

67 framework that assumes the soil pore system can be represented as two overlapping interacting regions, one which represents

68 the matrix domain with micropores and the other one represents the crack domain with meso-macro pores (Šimůnek et al.,

69 2003). Those models represent the cracks in the soil as implicit form which need not to prescribe geometrical and spatial

70 features of the desiccation cracks. The DPoM concept holds the simplifying stipulation that water only flows through the

71 shrinkage cracks rather than the soil matrix, which is unrealistic in many cases. To remedy this shortcoming, classical DPM

72 was developed, where, the water flow in soil matrix and crack domain was simulated using the Richards' equation (Aguilar‐

73 López et al., 2020; Coppola et al., 2012; Gerke and Maximilian Köhne, 2004; Gerke and Van Genuchten, 1993a) or Green-

74 Ampt model (Davidson, 1984; Stewart, 2019; Weiler, 2005) building on Darcy's law. However, some critics emerged that

75 the Richards' equation building on the capillarity, not existing in large PF paths (e.g. tensile cracks and biological holes), is

76 not suitable to simulate the PF (Larsbo and Jarvis, 2003; Nimmo, 2010; 2021). Consequently, some improved DPMs were

77 developed, where, water flow in the crack domain was simulated by the Navier-Stokes equation (Germann and Karlen, 2016;

78 Nimmo, 2010), kinematic wave equation (Greco, 2002; Larsbo and Jarvis, 2003) and Poiseuille model (Lepore et al., 2009).

79 Although these improved DPM models better captured the characteristics of the water flow in the crack domain, the classical

80 DPM concept has still been widely accepted and used in simulating preferential flow in soils due to its easily available

81  parameters, reasonably satisfactory prediction to the measurements and high computation efficiency (Jarvis et al., 2016). Most

82  importantly, a recent numerical study conducted by Aguilar‑López et al. (2020) proved that effective parameter selection in

83  the DPM models can achieve similar modeling results to the EMs.

84  Nevertheless, classical DPM models often adopt the assumption that crack volume and hydrological properties remain

85  constant in both time and space, which is unfeasible to capture the full dynamics of PF-DC. Some attempts have been made

86  to incorporate the dynamic nature of desiccation cracks into DPM including the SWAP family of models, i.e. LEACHM,

87  which simulates PF-DC using a shrinkage characteristic and water loss (Kroes et al., 2000), but neglects water exchange

88  process occurring at the interface between two domains. Such a process has widely been confirmed to be significant in cracked

89  soils (Greve et al., 2010; Krisnanto et al., 2016; Tuong et al., 1996). A later modification of SWAP incorporated the

90  aforementioned process, but at the cost of neglecting shrink-swell behavior of soil. The VIMAC model developed by Greco

91  (2002) solved previous problems but against the cost of inducing many parameters which are difficult to determine from

92  experiments or measurements. Coppola et al. (2012); (2015) took another step forward to allow crack volume and/or

93  hydrological properties to vary as a function of soil shrinkage. However, the relationship proposed in the model, an empirical

94  natural logarithm function involving the suction head and crack proportion, is not directly transferable to other types of soil. .

95  Stewart et al. (2016b) deduced a shrinking-swelling model, with relatively clear physical meaning and high consistency, and

96  recently incorporated it into a Green-Ampt based DPM (Stewart, 2018). While an analytical solution was obtained, the

97  intrinsic limitation of the Green-Ampt approach (i.e. hypothesis of the wetting front and request for a constant boundary

98  condition) hindered the further application of this model in complicated scenarios.

99  The objective of this research was to investigate the PF-DC from the experimental perspective in combination with an

100  effective modelling approach. Hence, a soil column test was conducted to investigate the dynamic changes of desiccation

101  cracks and hydrological response. The variation of crack geometry, including crack ratio, width and depth were measured.

102  The soil moisture content, matrix suction and water drainage were also monitored. Meanwhile, we developed a dynamic dual-

103  permeability preferential flow model by incorporating the shrinking-swelling model proposed by Stewart et al. (2016b). The

104  performance of the model was evaluated by comparing the simulated results with measured data.

105  **2.  Experimental study**

106  2.1 Testing apparatus

107  To investigate the effects of dynamic changes of desiccation cracks on preferential flow, a soil column infiltration test was

108  conducted under wetting-drying cycles (abbreviated as WD cycles hereafter). The testing apparatus consisted of a rainfall-

109  evaporation system, environment monitoring device, a plexiglass column, HD camera, hydrological sensors and drainage

110  measurement device (Fig. 1).

111  The rainfall-evaporation system included a rainfall simulator and two warm lamps as well as a small fan. The rainfall simulator

112  was 0.5 m above the soil surface, which can produce rainfall with the intensity of 24-120 mm/h. The warm lamps and a small

113  fan were put near the soil surface to accelerate water evaporation. The environment monitoring device consisted of a thermo-

114  hygrometer that connected a probe above the soil surface to detect the environmental temperature and humidity, and a water

115  container to measure the potential evaporation.

116  The plexiglass column was composed of a column (with a height of 60 cm and a diameter of 50 cm) placed on a catchment

117  hopper which was used to collect and drain out water from the soil column.

118  HD camera (TTQ-J2, constant focal length: 35 mm) was fixed on the slope above the soil surface to take photos at regular

119  intervals during the drying periods.

120  Hydrological sensors, including 5 soil moisture content/temperature sensors (Acclima, TDR-310s, with a measurement

121  moisture content range of 0-100%, an accuracy of ±2%; temperature range of -40 °C - +60 °C, an accuracy of ±0.2 °C) and 5

122  water potential sensors (Campbell, WP-257, with a measurement range of -200 kPa - 0 kPa, an accuracy of ± 0.5 kPa), were

123  used to monitor the hydrological response during WD cycles. Five TDR-310s and five WP-257s were inserted into the soil

124  column from the two opposite sides of the plexiglass column, respectively, with the same height spacing of 10 cm from top

125  to bottom.

126  Drainage measurement device, including two electronic balances, were used to record the cumulative water drainage from

127  the soil column.
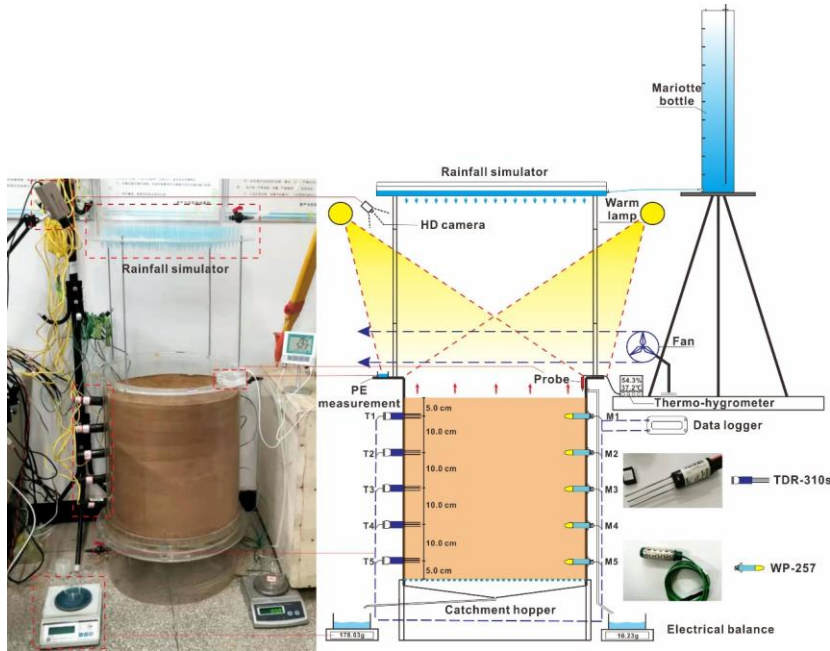
128

129  **Fig. 1** Schematic design and photos of the soil column test

130  2.2 Materials

131  The soil used in the test was taken from Zongyang county Anhui, China. Table 1 shows the basic physical parameters and

132  main mineral composition of the soil samples. The soil found in this study is classified as weak expansive soil. The saturated

133  hydraulic conductivity was measured on reconstituted soil cores with a dry density of $1.55 \text{g/cm}^3$ (the same as the soil column).

134  In addition, the shrinkage curve of the saturated soil core was also obtained using a similar method proposed in Wen et al.

135  (2021). The difference is that we measured the vertical deformation in regular time intervals instead of continuous monitoring.

136  Fig. 2 shows the variation of soil porosity with the volumetric water content.

137  **Table 1** Basic physical parameters of the soil sample

| Gs (-) | $\omega_{opt}$ | $\rho_{d,max}$ | $L_l$ (%) | $P_l$ (%) | $\delta_{ef}$ (%) | $C_{Illite}$ | $C_{Kaolinite}$ | $C_{Quartz}$ | $C_{Albite}$ | $K_s$ |
|---|---|---|---|---|---|---|---|---|---|---|
| 2.73 | 0.17 | 1.7 | 38.7 | 18.9 | 42.7 | 43-57 | 4-12 | 34-47 | 0-11 | $8.3\times10^{-7}$-$1.3\times10^{-6}$ |
| Gs - specific gravity (-); | | | | | | | | | | |
| $\omega_{opt}$ - optimal moisture content (g/g) which refers to the water content corresponding to the maximum dry density; | | | | | | | | | | |
| $\rho_{d,max}$ – the maximum dry density (g/cm³); | | | | | | | | | | |
| $L_l$ - liquid limit (%); $P_l$ - Plastic limit (%); | | | | | | | | | | |
| $\delta_{ef}$ - Free swelling ratio (%); | | | | | | | | | | |
| $C_{Illite}$, $C_{kaolinite}$, $C_{Quartz}$ and $C_{Albite}$ – content of illite, kaolinite, quartz and albite, respectively (%); | | | | | | | | | | |
| $K_s$ – Saturated hydraulic conductivity (m/s) | | | | | | | | | | |

138
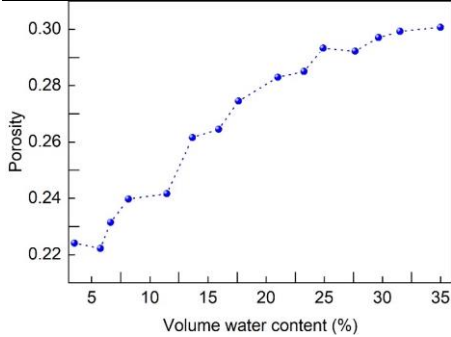
**Fig. 2** Shrinkage curve of the test soil

140 To ensure the homogeneity of the soil column, soil samples were compacted in 10 layers, and each layer was 5 cm thick. Prior

141 to filling soil into the plexiglass column, the soil samples with the total weight required for each layer were prepared according

142 to the designed density (dry density of 1.55g/cm³) and gravimetric water content (10%). Then, the soil samples were

143 compacted in the plexiglass column using a rubber hammer. The soil column was constructed within one day. After that, the

144 soil column was allowed to stand for 3 days to obtain stable records of the hydrological sensors.

145

146 2.3 Data collection

147 In the soil column test, the following data was collected:

148 (1) Boundary conditions: rainfall intensity ($r$, mm/h), potential evaporation ($PE$, mm/h) at 1 h time interval, temperature ($T$, ℃)

149 and relative humidity ($RH$, %) at 5 min time interval.

150 (2) Hydrological data: volume water content ($\theta_{exp}$, %) and soil matrix suction ($S_{exp}$, kPa) in different depths at 5 min time

151 interval, cumulative drainage from the top ($D_{top}$, g) and bottom ($D_{bottom}$, g) of the soil column.

152 (3) Crack geometric data: crack ratio ($w_{c,exp}$), crack aperture ($w_{j,exp}$), and the maximum crack depth ($d_{max}$, mm). The $w_{c,exp}$

153 and $w_{j,exp}$ were obtained via processing the crack photos which were taken at 20 min intervals during drying periods. The

154 image processing method mainly includes two steps as shown in Fig. 3. The $d_{max}$ was measured by thin wire before each

155 rainfall event.

156

157 Fig. 3 Process of crack image processing. (a) a photo obtained from the HD camera, 800 pixels × 1400 pixels; (b) crack

158 image after cropping and pixel enhancement, 1044 pixels × 1005 pixels; (c) crack image after binarization and denoise, and

159 the crack ratio was calculated as the crack area divided by the overall area of interest, the crack aperture was calculated as the

160 average value of crack aperture from three different positions.

161

162 2.4 Test procedure

163 The overall experimental process included two stages of WD cycles. The purpose of the first stage was to generate a relatively

164 stable surface pattern of the desiccation cracks. It started from 2022/01/05 15:00 to 2022/02/28 9:00, including thirteen WD

165 cycles.

166    The second stage started from 2022/02/28 9:00 to 2022/03/28 22:30, including seven WD cycles. Fig. 4 presents the variation

167    of rainfall, evaporation, temperature and relative humidity in the entire experiment process. Because the two warm lamps and

168    fan were closed during the night, two kinds of evaporation intensity can be observed during the drying periods. In addition,

169    the average environment temperature in the 5th WD cycle was higher because we turned up the power of the two warm lamps.

170    In this current study, we mainly focus on the second stage of WD cycles.
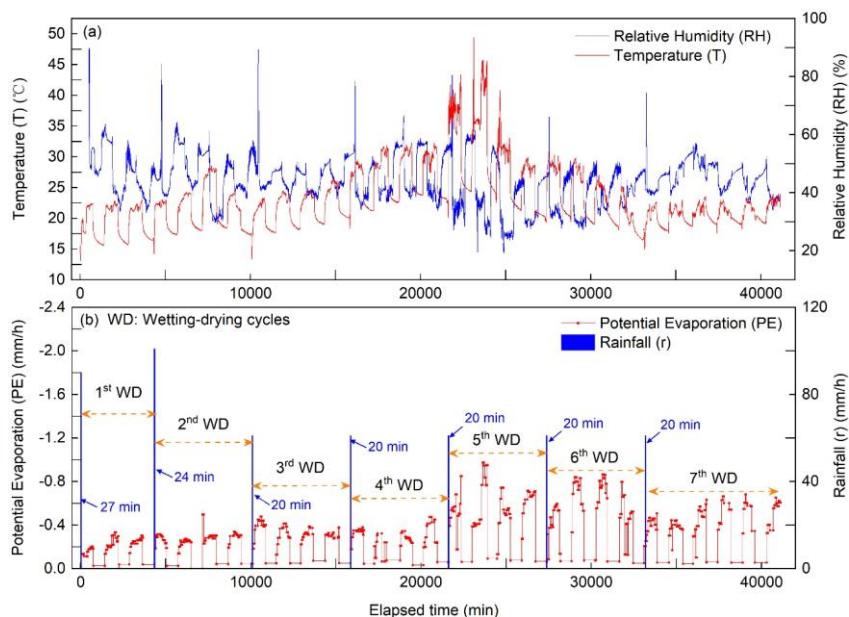
171

172    **Fig. 4** Environmental conditions of the experiment. (a) time series of temperature and relative humidity; (b) rainfall intensity

173    and potential evaporation.

174

175    **3.  Model Description**

176    3.1 Dual-permeability model (DPM)

177    The DPM concept used in this study corresponds to the one developed by Gerke and Van Genuchten (1993a). The model

178    divides the flow domain into two overlapping and interacting continua according to the volumetric ratios of each domain,

179    where two coupled 2-D Richards' equations are used to describe the matrix flow and preferential flow as

180    $$C_c(h)\frac{\partial h_c}{\partial t}=\nabla[K_c(h)\nabla(h_c+z)]-\frac{\Gamma_w}{w_c} \quad (1)$$

181    $$C_m(h)\frac{\partial h_m}{\partial t}=\nabla[K_m(h)\nabla(h_m+z)]+\frac{\Gamma_w}{w_m} \quad (2)$$

182    $$\Gamma_w=\alpha_w K_a(h_c-h_m) \quad (3)$$

183    $$w_c+w_m=1 \quad (4)$$

184    where subscript "$c$" and "$m$" indicate the crack and matrix domains, respectively; $h$ (m) is the pressure head; $C$ represents the

185    specific water capacity, $d\theta/dh$ (1/m); $\theta$ (-) is the volumetric water content; $K$ (m/s) is the isotropic hydraulic conductivity;

186    $z$ (m) is the elevation head; $w$ (-) is the volumetric ratio of the crack domain or matrix domain over the bulk soil volume;

187    $\Gamma_w$ is the water exchange term (1/s) between the two domains; $\alpha_w$ (1/m²) is the effective water transfer coefficient; $K_a$

188 (m/s) is the interface hydraulic conductivity.

189 The hydraulic properties of the two domains are parameterized based on the Mualem-van Genuchten soil-water retention

190 curves (SWRC) (Mualem, 1976; Van Genuchten, 1980) as

191 $S_e(h) = \dfrac{\theta - \theta_r}{\theta_s - \theta_r} = \left[1 + (|\alpha h|)^n\right]^{-m}$    (5)

192 $K(S_e) = K_s K_r(S_e) = K_s S_e^{0.5}[1 - (1 - S_e^{1/m})^m]^2$    (6)

193 where $S_e$ (-) is the effective saturation; $\theta_s$ (-) and $\theta_r$ (-) are the saturated and residual volumetric water content, respectively;

194 $\alpha$ (1/m), $n$ (-) and $m$ (-) are fitting parameters; $K_s$ (m/s) is the saturated hydraulic conductivity; $K_r$ (-) is the relative

195 hydraulic conductivity.

196 According to Gerke and Van Genuchten (1993a), the total porosity $\varepsilon$ (-), total volume water content $\theta$ (-), total hydraulic

197 conductivity $K$ (m/s) and total volumetric flux (m/s) in terms of the volume ratio of each domain can be expressed as

198 $\varepsilon = w_c \varepsilon_c + w_m \varepsilon_m$    (7)

199 $\theta = w_c \theta_c + w_m \theta_m$    (8)

200 $K = w_c K_c + w_m K_m$    (9)

201 Note that the total porosity $\varepsilon$ is define as the total pore volume ($V_p$) divided by total soil volume ($V$), while $\varepsilon_m$ ( or $\varepsilon_c$ ) is

202 defined as the pore volume in matrix ($V_{p,m}$) (or crack, $V_{p,c}$) domain divided by the volume of that domain ($V_m$ or $V_c$). The total

203 volume water content has the same definition.

204 In the case of a DPM model, specified flux $i$ is divided between the matrix and crack domains as

205 $i = w_c i_c + w_m i_m$    (10)

206 where $i_c$ and $i_m$ are the effective boundary fluxes into each domain (m/s).

207 Considering a rainfall condition, the effective boundary fluxes of the two domains are initially equal to rainfall intensity ($r$)

208 due to the infiltration capacity of each domain is larger than $r$ (Dusek et al., 2008), and therefore the boundary fluxes of each

209 domain can be written as

210 $i_c = r$    (11)

211 $i_m = r$    (12)

212 As the soil keeps wetting, the decrease of the pressure head gradient may firstly lead to the infiltration capacity of matrix

213 domain dropping to a value less than $r$. Then, ponding occurs on the surface of the soil matrix and the boundary condition

214 changes to a specified pressure head boundary. This transformation can be achieved in COMSOL, a multi-physic solver and

215 simulation software package building on finite element method, by using a combined type of boundary (Dirichlet and

216 Neumann) proposed by Chui and Freyberg (2009). Once ponding occurs on the matrix domain, the surplus water from that

217 domain infiltrates into the crack domain and its effective flux increases to

218 $i_c = (r - w_m i_m) / w_c$    (13)

219 when the retained water volume in the cracks exceeds its storage capacity, water will pond on the surface of the crack domain.

220 Considering an evaporation condition, the Wilson-Fredlund-Barbour-Penman experimental function model (Wilson et al.,

221 1997) was used to calculate the actual evaporation of each domain

222 $AE / PE = \exp\left(\dfrac{-Sg\omega_v}{\xi(1 - h_a)\gamma_w R(T_s + 273.15)}\right)$    (14)

223 where AE is the actual evaporation; PE is the potential evaporation measured in the experiment; $S$ (kPa) is total matric suction

224 at the soil surface; $g$ (m/s$^2$) is the gravitational acceleration constant; $\omega_v$ is molecular mass of water, 0.018kg/mol; $\xi$ is

225  a dimensional empirical parameter with a suggested value of 0.7; $h_a$ is relative humidity of overlying air; $\gamma_w$ is unit mass

226  of water, 9.807 kN/m³; R is universal gas constant, 8.314J/(mol·K); $T_s$ (℃) is the soil surface temperature.

227

228  3.2 Dynamic dual-permeability model (DPMDy)

229  3.2.1 Porosity description

230  In Stewart et al. (2016a); (2016b) and Stewart (2018), the total porosity ($\phi_{max}$) of a cracked soil was divided into three domains:

231  aggregates (or soil matrix), cracks (voids from horizontal deformation induced by desiccation cracks) and subsidence (voids

232  from vertical deformation induced by desiccation cracks). In Stewart et al. (2016a), the distributions of these domains change

233  as a function of a unified water content, $U$

234  $$\phi_{max} = \phi_{matrix}(U) + \phi_{crack}(U) + \phi_{sub}(U) \qquad (15)$$

235  where the subscripts matrix, crack and sub refer to the aforementioned three domains. In this study, we assume that the

236  horizontal deformation dominates the formation of desiccation cracks, thus $\phi_{sub}(U)$ can be neglected.

237  Stewart et al. (2016a) then deduced the porosities of each domain as:

238  $$\phi_{matrix}(U) = (\phi_{max} - \phi_{min})(\frac{p+1}{p+U^{-q}}) + \phi_{min} \qquad (16)$$

239  $$\phi_{crack}(U) = (\phi_{max} - \phi_{min})(\frac{1-U^q}{1+pU^q}) \qquad (17)$$

240  where $p$ and $q$ are functional shape parameters; $\phi_{max}$ is the maximum porosity of a soil core prior to shrinkage and thus also

241  represents the total porosity; $\phi_{min}$ is the minimum porosity of the matrix domain; $U$ is a unified water content (defined as

242  water content $u$ divided by its saturated value $u_{max}$), which can be approximately estimated to be the saturation degree ($S_{e,m}$)

243  in an SWRC function of the soil matrix (Stewart et al., 2016a). Indeed, Eq. (16) represents a shrinkage curve function in which

244  four parameters can be obtained through a shrinkage test.

245  Substituting $S_{e,m}$ as $U$ and incorporating Eq. (5) into Eq. (16) and Eq. (17), we can obtain the porosity of the two domains as

246  a function of pressure head $h$

247  $$\phi_{matrix}(h) = (\phi_{max} - \phi_{min})(\frac{p+1}{p+S_{e,m}^{-q}}) + \phi_{min} = (\phi_{max} - \phi_{min})(\frac{p+1}{p + \left(\left[1+(|\alpha_m h_m|)^{n_m}\right]^{-m_m}\right)^{-q}}) + \phi_{min} \qquad (18)$$

248  $$\phi_{crack}(h) = (\phi_{max} - \phi_{min})(\frac{1-S_{e,m}^q}{1+pS_{e,m}^q}) = (\phi_{max} - \phi_{min})(\frac{1-\left(\left[1+(|\alpha_m h_m|)^{n_m}\right]^{-m_m}\right)^q}{1+p\left(\left[1+(|\alpha_m h_m|)^{n_m}\right]^{-m_m}\right)^q}) \qquad (19)$$

249  With these porosity equations in mind, we can rewrite Eq. (4) and Eq. (7) as:

250  $$\phi_{max} = w_c \varepsilon_c + (1-w_c)\varepsilon_m \qquad (20)$$

251  Because the crack domain is mainly composed of voids, we here assume that $V_{p,c}$ equals to $V_c$, and thus $\varepsilon_c = 1$. Through this

252  assumption, we obtained a physically-consistent definition of how the porosity and crack volume vary as functions of

253  saturation degree as follow

254  $$w_c \varepsilon_c = w_c = \phi_{crack}(S_{e,m}) = (\phi_{max} - \phi_{min})(\frac{1-S_{e,m}^q}{1+pS_{e,m}^q}) \qquad (21)$$

255  $$\varepsilon_m = \frac{\phi_{matrix}(S_{e,m})}{1-w_c} = \left[(\phi_{max} - \phi_{min})(\frac{p+1}{p+S_{e,m}^{-q}}) + \phi_{min}\right] / \left[1 - (\phi_{max} - \phi_{min})(\frac{1-S_{e,m}^q}{1+pS_{e,m}^q})\right] \qquad (22)$$

256

### 3.2.2 Water content and hydraulic conductivity

In terms of Eq. (8), the total water content of the soil volume can be expressed as:

$$\theta = \phi_{crack}(h)\theta_c + (1-\phi_{crack}(h))\theta_m \quad (23)$$

Regarding the hydraulic conductivity of each domain, the classical DPM often assumed it equals to the product of a fixed Ks and the relative hydraulic conductivity $K_r$ of the corresponding domain. In the DPMDy model, VG-Mualem equation is adopted in the matrix domain, while in the cracks, where capillarity has little effect on water flow, we set $K_r$=1. Hence, the following equations are obtained

~~Regarding the hydraulic conductivity of each domain, the classical DPM often assumed it equals to the product of a fixed $K_s$ and the relative hydraulic conductivity of the corresponding domain. The following equations are obtained according to Eq. (6).~~

$$\begin{cases} K_m = K_{m,s}K_r(S_{e,m}) = K_{m,s}S_{e,m}^{\,0.5}[1-(1-S_{e,m}^{\,1/m_m})^{m_m}]^2 \\ K_c = K_{c,s}K_r(S_{e,c}) = K_{c,s}S_{e,c}^{\,0.5}[1-(1-S_{e,c}^{\,1/m_c})^{m_c}]^2 \end{cases} \quad (24)$$

~~$K_c = K_{c,s}K_r(S_{e,c}) = K_{c,s}S_{e,c}^{\,0.5}[1-(1-S_{e,c}^{\,1/m_c})^{m_c}]^2$ (24)~~

~~$K_c = K_{c,s}K_r(S_{e,c}) = K_{c,s}S_{e,c}^{\,0.5}[1-(1-S_{e,c}^{\,1/m_c})^{m_c}]^2$~~ $K_c = K_{c,s}$ (25)

where $K_{c,s}$ and $K_{m,s}$ refer to the saturated hydraulic conductivity in crack and matrix domains, respectively.

However, the $K_{c,s}$ and $K_{m,s}$ are transient variables that changes with the crack geometries in crack domain and porosity in matrix domain, which should be taken into consideration in a shrinking-swelling soil. To solve this issue, Stewart et al. (2016b) further deduced models that describe the relationships between $K_{m,s}$, $K_{c,s}$ and $S_{e,m}$.

$$K_{m,s}(S_{e,m}) = K_{m,\max}\left(\frac{p+1}{p+S_{e,m}^{\,-q}}\right) \quad (26)$$

$$K_{c,s}(S_{e,m}) = K_{c,\max}\left(\frac{1-S_{e,m}^{\,q}}{1+pS_{e,m}^{\,q}}\right)^2 \quad (27)$$

where $K_{c,\max}$ is the maximum saturated hydraulic conductivity of the crack domain (at $S_{e,m}$ = 0) when the crack aperture achieves the maximum value; $K_{m,\max}$ is the maximum saturated hydraulic conductivity of the matrix domain (at $S_{e,m}$ = 1) when the radius of cylindrical pores in that domain achieves the maximum value (See Eq. (25) and Eq. (27) in Stewart et al. (2016b)). The assumption $K_r(S_{e,c})$ =1 means that the magnitude of ~~In the DPMDy model, we here set $K_r(S_{e,c})$ to 1 in Eq. (25). This modification means that the magnitude of~~ $K_c$ only depends on the crack area or the saturated degree of the soil matrix domain.

$$K_c = K_{c,s} = K_{c,s}(S_{e,m}) = K_{c,\max}\left(\frac{1-S_{e,m}^{\,q}}{1+pS_{e,m}^{\,q}}\right)^2 \quad (28)$$

Incorporating Eq. (26) and Eq. (27) into Eq. (9) obtains:

$$K_s = \phi_{crack}(h)K_{c,\max}\left(\frac{1-S_{e,m}^{\,q}}{1+pS_{e,m}^{\,q}}\right)^2 + (1-\phi_{crack}(h))K_{m,\max}\left(\frac{p+1}{p+S_{e,m}^{\,-q}}\right) \quad (29)$$

Note that $K_{m,\max}$ can be obtained by laboratory-based infiltration test through a saturated soil core prior to shrinkage. Then,

286  Eq. (29) can be used to fit the $K_{c,\max}$ through the overall saturated hydraulic conductivity (measured $K_s$) under different

287  crack volume or ratio. Alternatively, $K_{c,\max}$ can also be approximately calculated as

288  $$K_{c,\max} = \frac{w_{j,\max}{}^2 g}{12v} \qquad (30)$$

289  where $w_{j,\max}$ stands for the maximum crack aperture measured in experiment (m), g is the gravity acceleration constant

290  (m/s$^2$), and $v$ is the water kinematic viscosity (m$^2$/s). This equation is a relation to the cubes of the aperture of a crack with

291  respect to the crack inner flux, which is based on the derivation of laminar flow between parallel plates for Hagen-Poiseuille

292  type of flow (Snow, 1965).

293  Eventually, we can simulate the hydrological process with considering the dynamic changes of desiccation cracks by

294  incorporating Eq. (19), Eq. (21), Eq. (26), Eq. (27) and Eq. (28) into the DPM.

295

296  ## 4.  Experimental results

297  4.1 Crack dynamic changes

298  Fig 5 presents typical images of crack evolution during each WD cycle. Intuitively, it seems that the crack area and width did

299  not show an obvious increasing trend with the WD cycles as expected. Conversely, during the 1st to 4th WD cycles, the cracks

300  at the same moment after rainfall (Fig 5b2-4) and the final state (Fig 5c2-4) decreased significantly even though the

301  environmental temperature ($T$) and the potential evaporation ($PE$) increased in these periods. The cracks increased

302  significantly since the 5th WD cycle, but most of them were finer than before. Overall, cracks in the 1st WD cycle are wider

303  than those formed in other cycles.

304
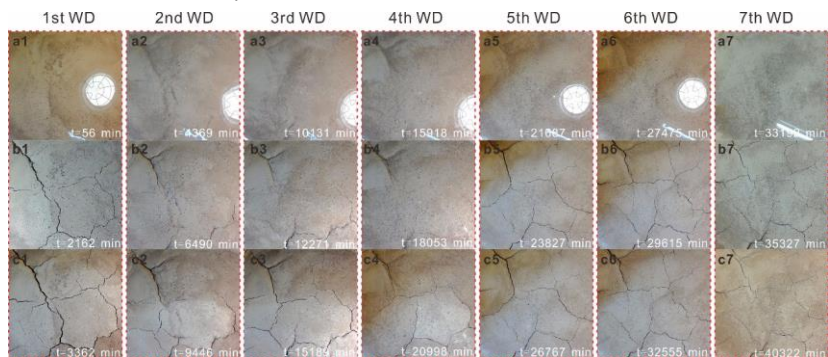
305  **Fig. 5** Typical images of crack evolution in seven wetting-drying cycles. (a1-7) water ponds on the soil surface after rainfall;

306  (b1-7) crack images at the 2135th min after each rainfall; (c1-7) crack images at the end of the final high evaporation period

307  during each wetting-drying cycle

308

309  Fig 6 quantitatively shows the variation of crack ratio ($w_{c,exp}$) and crack aperture ($w_{j,exp}$) in the experiment. Overall, the

310  variation curves corresponded to the intuitive descriptions mentioned above. Especially, an unexpected result was that the $T$

311  and $PE$ in the 5th and 6th WD cycles were higher than in previous cycles, but their maximum $w_{c,exp}$ and $w_{j,exp}$ became

312  smaller. During a single WD cycle, the $w_{c,exp}$ and $w_{j,exp}$ have a similar trend, which shows a dramatic decrease during

313  rainfall, rapid increase in high evaporation periods and slow increase or even decrease in low evaporation periods. More

314  specifically, during the rainfall periods, the crack closure process was not significant until the water ponded on the soil matrix,

315    then ponded water flowed into the cracks, leading to acceleration of the crack closure. Note that cracks were not completely

316    closed even when they were full of water (Fig 5a1-7). The minimum crack ratio under such conditions is approximately 0.1%.

317    In the evaporation periods, the maximum crack ratio reaches 2.87% and the maximum crack aperture reaches 2.6 mm. In

318    addition, Fig 7 shows the maximum crack depth ($d_{max}$) measured after each cycle. It can be seen that $d_{max}$ increased

319    substantially after the 1st WD cycle and then slightly increased in the last six cycles, with a maximum value of 23.8 cm.
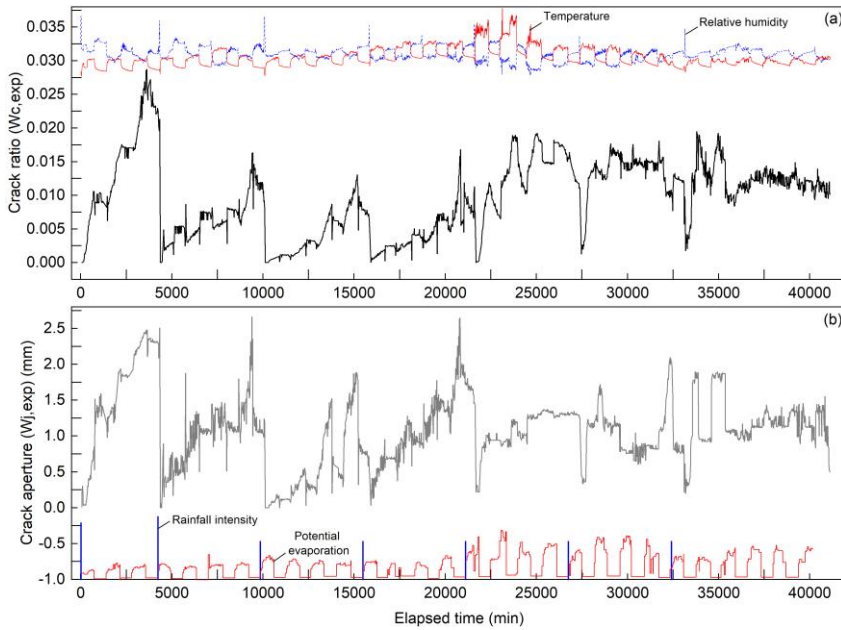
320

321    **Fig. 6** Time series of crack geometries. (a) crack ratio; (b) crack aperture
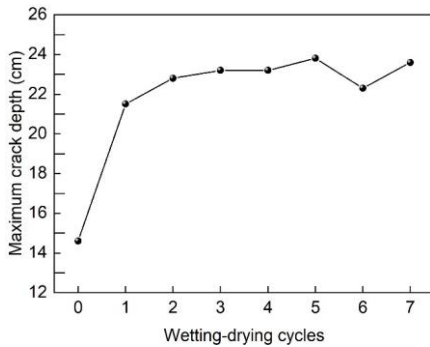
322

323    **Fig. 7** The maximum crack depth measured after each wetting-drying cycle

324

325    4.2 Hydrological response

326    Table 2 presents the manually recorded results of external hydrological responses involving ponding and drainage during each

327    WD cycle. It can be seen that the ponding occurred on the soil surface within 5 min after each rainfall. The ponding duration

328    in each rainfall mainly decreased with WD cycles. Note that the ponding depth in each rainfall was below the upper drainage

329    outlet. Regarding the water drainage, approximately 1.4 kg of water (the total water mass was 8 kg) was leaked during the 1st

330    rainfall due to the interspace between the soil and the plexiglass column and the hydrological sensors. Then, we sealed the

331 interspace using clay powder and polyurethane cement (soft materials without constrain effects on the soil swelling) after

332 each drying process, and subsequently, no water drainage was observed at the bottom outlet.

333 **Table 2** Manual readings of external hydrological responses

| Wetting-drying cycles | 1st | 2nd | 3rd | 4th | 5th | 6th | 7th |
|---|---|---|---|---|---|---|---|
| $t_p$ (min) | 4.1 | 1.8 | 1.2 | 1.2 | 1.2 | 2.2 | 2.8 |
| Ponding duration (min) | 70 | 160 | 68 | 47 | 34 | 25 | 23 |
| Drainage (g) | 1412 | - | - | - | - | - | - |
| *$t_p$ (min) – beginning of ponding after each rainfall | | | | | | | |

334 Fig 8 shows the internal hydrological responses recorded by the soil moisture and water potential sensors. Because the M2

335 and M4 were damaged during soil compaction, no matric suction data was obtained at their depths. Overall, water content at

336 all depths increased during rainfall and decreased during evaporation, where T1 showed the most sensitive responses to the

337 WD cycles. During rainfall, the time for water content to respond to each rainfall increased with depths, but the time difference

338 among all depths decreased significantly since the 2nd WD cycle. During the drying periods, an interesting phenomenon was

339 that the water content at 5 cm depth showed an overall decline trend, but transient increases of water content frequently

340 appeared during low evaporation periods. Such transient increases seem to be related to the slow decrease of crack ratio as

341 mentioned in section 4.1. Regarding the matric suction, its variation trend was similar to the water content but showed more

342 delayed responses to the environmental conditions, especially in the last three WD cycles. Additionally, Fig 8b also implies

343 that soil at 5 cm depth reached saturation during each rainfall, while soil below the 25 cm depth was in the unsaturated state

344 in the whole experiment process.

345
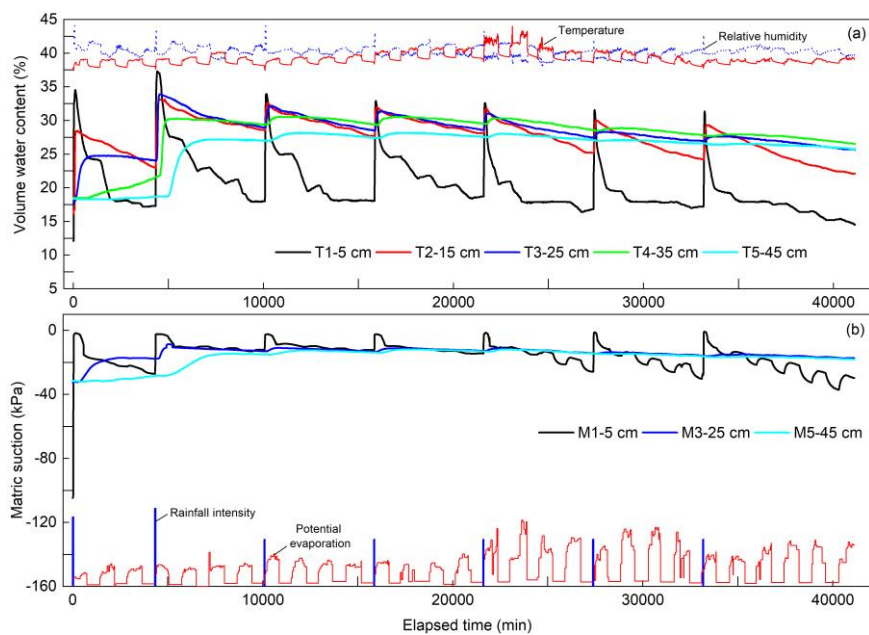
346 **Fig.8** Time series of volume water content (a) and matric suction (b) at different depths.

347

348 **5. Numerical simulation**

349 5.1 Set-up of numerical model

350 The single-domain model (SDM), dual-permeability model (DPM) and dynamic DPM (DPMDy) were implemented in a finite

351   element solver for Richards' equation as part of the COMSOL Multiphysics software (Comsol 5.6). As shown in Fig 9, they

352   have the same 2-D size, boundary conditions, mesh structure and initial condition. The model domain is 0.5 m by 0.5 m, same

353   as the soil column. Because the measured maximum crack depth was 23.8 cm, we specified the crack domain existing within

354   the upper 25 cm depth of the soil column.

355   The boundary conditions at the top were set as combined type of boundary conditions (as mentioned in section 3.1) for

356   representing the rainfall, ponding and evaporation process recorded in the experiment; the bottom side is a seepage boundary

357   condition; the left and right sides of the model are no-flux boundaries.

358   Because the pressure head in the surface area may change frequently and drastically during WD cycles, a refined mesh

359   structure with dense boundary layers was used to capture the transient hydrological conditions. The boundary layers included

360   15 layers of rectangular grid, with the minimum and maximum thick of approximately 0.04 cm and 0.3 cm, respectively. A

361   coarser free-triangle mesh (average length of 1.8 cm) was defined below the boundary layers. The initial condition both in

362   matrix and crack domains was set as the distribution of pore water pressure measured from the experiment prior to the 1st WD

363   cycle.

364
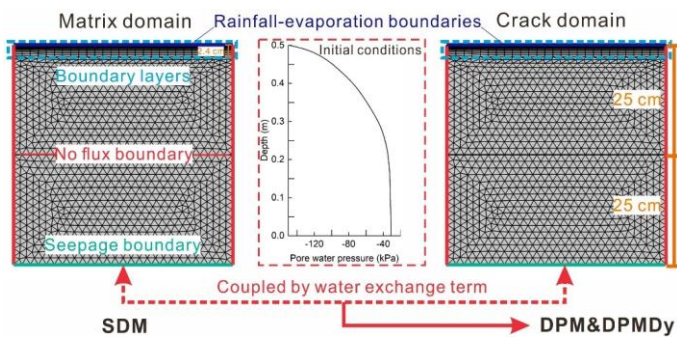
365   **Fig. 9** Set-up of the 2-D numerical model for the SDM, DPM and DPMDy

366

367   5.2 Parameters

368   5.2.1 Shrinkage parameters

369   As shown in Fig 10, using Eq. (18) to fit the measured shrinkage curve in Fig. 2, we obtained the four shrinkage parameters

370   as $\phi_{min}=0.22$, $\phi_{max}=0.30$, $p=8.8\pm4.84$, $q=2.71\pm0.85$. Then, the variation of porosity in crack domain (or crack ratio

371   $w_c$) and matrix domain ($\varepsilon_m$) could be obtained using Eq. (21) and Eq. (22), respectively. Note that the minimum $w_c$ calculated

372   by Eq. (21) was set as 0.001 considering the incomplete closure of cracks during rainfall.

373
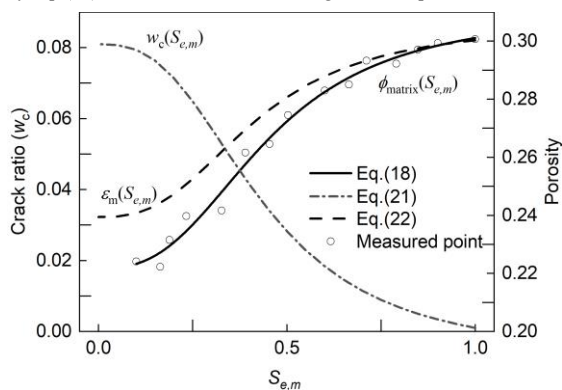
**Fig. 10** Fitted shrinkage curve (solid line) and modeled porosity variation of matrix (dash line) and crack domains (dash-dot line)

5.2.2 Soil water retention parameters

**Fig 11** shows the measured matric suction versus volume water content at different depths. The SWRCs were estimated using best fitting of the van Genuchten-Mualem equation to measured soil water retention data. It can be seen that the WD cycles lead to hysteretic curves in the SWRC at 5 cm and 25 cm depths, while that at the 45 cm depth rarely show hysteretic curves. This result may also indicate that most of the cracks exist within the upper 25 cm depth of the soil column. In this study, we simply estimated an approximate single SWRC of the soil matrix through experiment data instead of incorporating the hysteretic curves into the model. For instance, the estimated SWRC curve in **Fig 11a** lies between the wetting SWRC and drying SWRC to capture the overall characteristics of wetting-drying SWRC as far as possible. Note that the shape parameter $n$ in the upper matrix domain is slightly smaller than the lower one considering the upper soil matrix may become denser after long-time WD cycles (13 times, 54 days). Regarding the SWRC of the crack domain, as we assume the crack domain does not contain any solids, the

saturated water content ($\theta_{c,s}$) and the residual water content ($\theta_{c,s}$) of that domain was set to be 0.99 and 0.01, respectively. Meanwhile, because SWRC of the crack domain cannot be experimentally determined, we assigned the other two SWRC parameters ($a$=1.5 and $n_c$=2) to mimic coarse textured soil like behavior, and to be consistent with Poiseuille law-, which implies little effects of capillarity on flow through the cracks~~which implies that we neglect capillarity in the cracks~~.
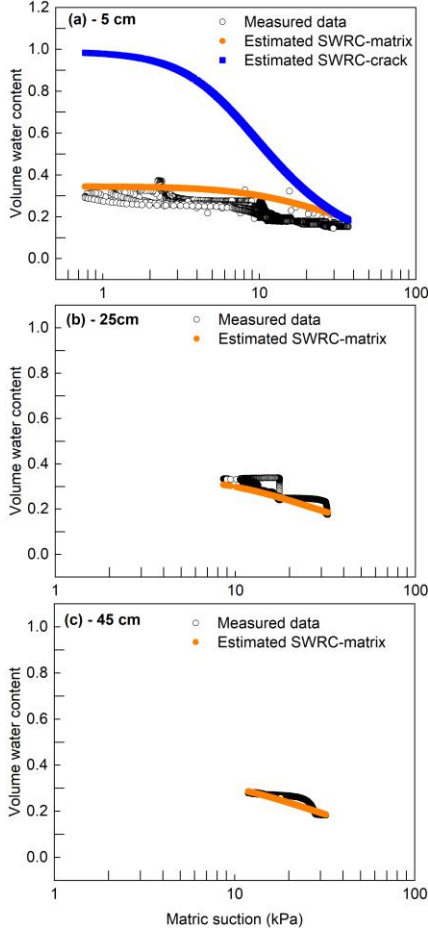
392

393    **Fig. 11** Measured and estimated SWRC at different depths. (a) 5 cm; (b) 25 cm; (c) 45 cm

394

395    5.2.3 Hydraulic conductivity

396    As mentioned in Eq. (29), the maximum saturated hydraulic conductivity of matrix domain ($K_{m,max}$) equals the saturated

397    hydraulic conductivity ($K_s$) measured in laboratory. Here, we set $K_{m,max} = 1.16 \times 10^{-6}$ m/s. Regarding the $K_{c,max}$, it was

398    calculated using Eq. (30), where the $w_{j,max}$ was set to 2.6 mm obtained from Fig 6b. Then, the variation curve of transient

399    saturated hydraulic conductivity of the matrix domain ($K_{m,s}$) and the crack domain ($K_{c,s}$) could be obtained using Eq. (27)

400    and Eq. (28), respectively. Note that here we slightly modified Eq. (28) as follow.

401    $$K_{c,s}(S_{e,m}) = K_{c,max}\left(\frac{1 - S_{e,m}^{\ q}}{1 + pS_{e,m}^{\ q}}\right)^2 + K_{c,min} \quad (28\text{-}b)$$

402    This modification not only avoided the $K_{c,s}$ dropping to zero thus benefits the numerical convergence, but also was

403    reasonable when considering the incomplete closure of cracks during rainfall. The $K_{c,min}$ was also estimated using Eq. (30)

404    with a suggested $w_{j,max} = 0.01$ mm. Further, the variation of $K_m$ and $K_c$ with the pressure head ($h$) in the DPMDy could

405    be calculated by combining Eq. (24), Eq. (26) and Eq. (28). **Fig 12** presents $K_m$ and $K_c$ in the three models. Note that the

406  pressure head in $K_c(h_m)$ of the DPMDy refers to that of the matrix domain ($h_m$), while $h$ in $K_c(h_c)$ of the DPM refers to
407  that of the crack domain ($h_c$).
408
409  5.2.4 Water exchange between and pore domains
410  In the dual-permeability concept, another important parameter is the hydraulic conductivity of the interface between matrix
411  and crack domains ($K_a$). Generally, $K_a$ was often estimated as the arithmetic mean of hydraulic conductivity of the two domains
412  (Arora et al., 2011; Coppola et al., 2012; 2015; Gerke and Van Genuchten, 1993b; Laine-Kaulio et al., 2014; Shao et al., 2015).
413  However, this approximation may overestimate the $K_a$ when the hydraulic conductivity of the crack domain is much higher
414  than that of the matrix domain, especially in cracked clays. In our current study, a $K_a$ function reformulated by (Gerke et al.,
415  2013) was adopted.

416
$$K_{a_{min}} = \begin{cases} \min\{K_m(h_c), K_c(h_c)\} & h_c \geq h_m \\ \min\{K_m(h_m), K_c(h_m)\} & h_c < h_m \end{cases} \qquad (31)$$

417  This formulation represents that the flow occurs from the highest head toward the lowest head but regulated by the less
418  permeable of the two subsystems in that instant of time (Aguilar‐López et al., 2020).
419  Regarding the $\alpha_w$, experimental results presented by Song et al. (2018) showed that the saturated $K_a$ may be 1 order of
420  magnitude larger than the $K_{m,s}$ which will represent an enlarging coefficient ranging from 10 to 18. Hence, the $\alpha_w$ was set
421  as 10 m$^{-2}$ considering the saturated $K_{a_{min}}$ determined by Eq. (31) equals to the $K_{m,s}$.
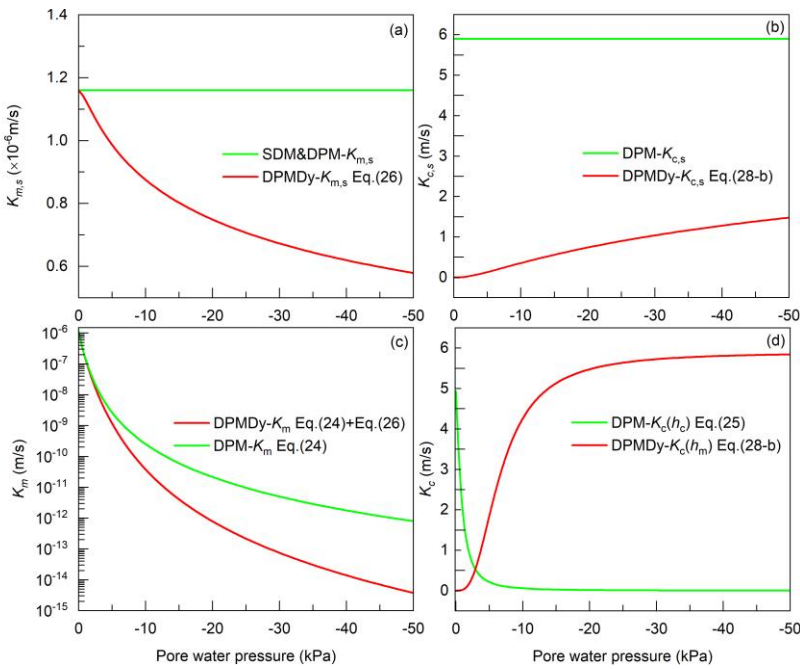
422
423  **Fig. 12** Modeled hydraulic conductivity of each domain in the three models. (a) Saturated hydraulic conductivity of the matrix
424  domain; (b) saturated hydraulic conductivity of the crack domain; (c) transient hydraulic conductivity of the matrix domain;
425  (d) transient hydraulic conductivity of the crack domain
426
427  All parameters and parametric methods for the SDM, DPM and DPMDy are listed in **Table 3**.

428 **Table 3** Summary of parameters and parametric methods for the SDM, DPM and DPMDy

| Model | Symbol | Parameter name | Units | Upper layer | Lower layer | Parameterization |
|---|---|---|---|---|---|---|
| SDM DPM DPMDy | $\theta_{m,s}$ | Saturated water content of matrix domain | (-) | 0.345 | 0.345 | Fitting to data |
| | $\theta_{m,r}$ | Residual water content of matrix domain | (-) | 0.01 | 0.01 | Fitting to data |
| | $\alpha_m$ | SWRC fitting parameter of matrix domain | (1/m) | 0.6 | 0.6 | Fitting to data |
| | $n_m$ | SWRC fitting parameter of matrix domain | (-) | 1.65 | 1.8 | Fitting to data |
| | $K_{m,max}$ | The maximum $K_s$ of matrix domain | (m/s) | $1.16 \times 10^{-6}$ | $1.16 \times 10^{-6}$ | Measured |
| DPM DPMDy | $\theta_{c,s}$ | Saturated water content of crack domain | (-) | 0.99 | - | Assigned |
| | $\theta_{c,r}$ | Residual water content of crack domain | (-) | 0.01 | - | Assigned |
| | $\alpha_c$ | SWRC fitting parameter of crack domain | (1/m) | 1.5 | - | Assigned |
| | $n_c$ | SWRC fitting parameter of crack domain | (-) | 2 | - | Assigned |
| | $K_{c,max}$ | The maximum $K_s$ of crack domain | (m/s) | 5.9 | - | Measured |
| | $K_a$ | Hydraulic conductivity of the interface | (m/s) | $K_{amin}$ | - | Assigned |
| | $a_w$ | Mass transfer coefficient | (1/m²) | 10 | - | Assigned |
| DPMDy | $\phi_{max}$ | The maximum porosity of a soil core | (-) | 0.3 | - | Fitting to data |
| | $\phi_{min}$ | The minimum porosity of a soil core | (-) | 0.22 | - | Fitting to data |
| | p | Shape parameter of soil shrinkage curve | (-) | 10 | - | Fitting to data |
| | q | Shape parameter of soil shrinkage curve | (-) | 3.5 | - | Fitting to data |
| DPM | $w_c$ | Constant crack ratio using in DPM | (-) | 0.01; 0.03 | - | Assigned |
| * SDM: single-domain model; DPM: dual-permeability model neglecting crack dynamic changes; DPMDy: Dynamic DPM; $w_c$ = 0.01 and 0.03 refers to the average and the maximum value of the measured crack ratio, respectively. | | | | | | |

429

430 5.3 Simulation results

431 5.3.1 Boundary flow

432 **Fig. 13** shows the temporal evolution of the boundary flow velocity simulated by the SDM, DPM and DPMDy. As shown in

433 **Fig. 13a1 and a3**, during drying periods, the matrix domain dominates the soil evaporation process and was responsible for

434 97%-99% of the total evaporation in all the dual-permeability models. The matrix evaporation rate ($e_m$) simulated by the

435 DPMDy was overall lower than that of the SDM and DPM during high-intensity evaporation periods, but the crack

436 evaporation rate ($e_c$) simulated by the DPMDy, especially during the last three drying periods, was approximately one to two

437 orders of magnitude larger than that of the DPM (see the enlarged image in Fig. a1).

438 With regard to the wetting process, **Fig. 13a2 and a4** represent two typical infiltration patterns before and after the 5th drying

439 period (with significantly increased evaporation intensity). Overall, matrix flow still dominated the infiltration process in all

440 the dual-permeability models due to the relatively small crack ratio and depth. For the SDM, all the rainfall infiltrates into the

441 soil during the beginning of rainfall events. When the soil surface gets saturated, water ponding occured and the soil infiltration

442 rate gradually decreased. In the DPM and DPMDy, the surplus water after matrix ponding infiltrates into the crack domain as

443 preferential flow, and water will pond on the overall soil surface when the crack domain reached its storage capacity. Recall

444 that the crack volume in the DPMDy decreases with the matrix getting moist, while that in the DPM keeps constant.

445 Consequently, the ponding time of the crack domain simulated by the DPMDy in the 3nd rainfall event (inflection point of the

446 red dash line in Fig. 13a2) was 1.6 and 4.8 min earlier than that of the DPM-0.01 and DPM-0.03, respectively. The cumulative

447 preferential flow simulated by the DPMDy was 87.4% and 95.2 % less than that of the DPM-0.01 and DPM-0.03, respectively.

448 Similar rainfall pattern was obtained during the 6th rainfall event.
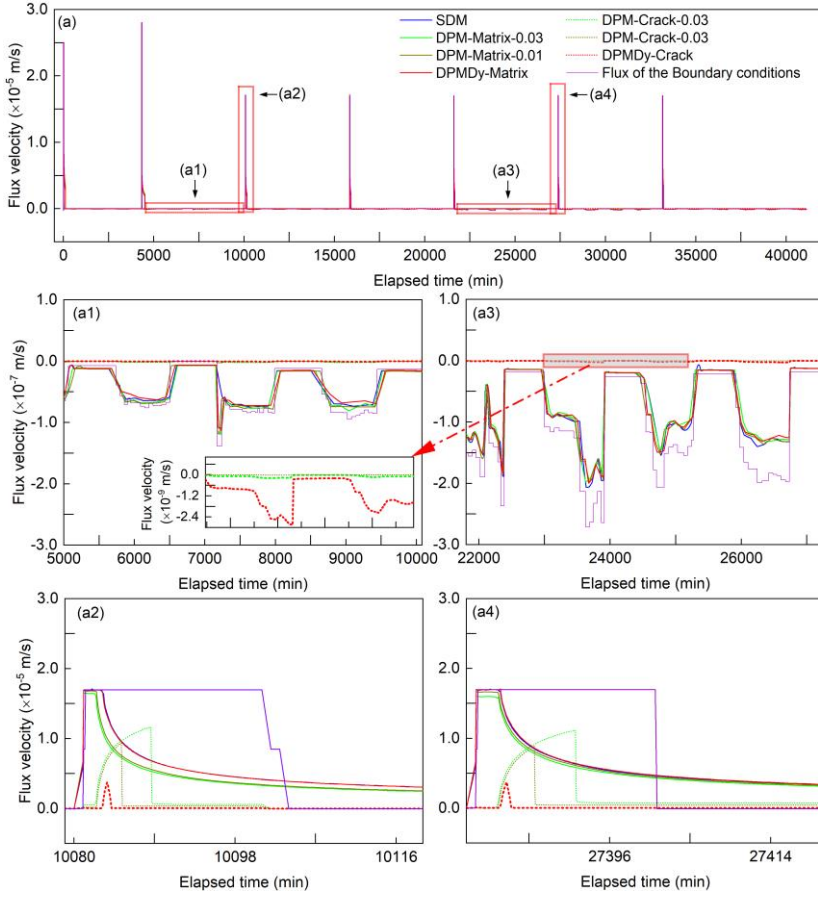
449
450 **Fig. 13** Boundary flow simulated by the SDM, DPM and DPMDy. (a) Flow velocity of the boundary conditions and simulated
451 results; (a1) and (a2) are the enlarged images of the flow velocity during the 2st drying and 3nd wetting process, respectively;
452 (a3) and (a4) are the enlarged images of the flow velocity during the 5th drying and 6th wetting process, respectively. The
453 positive value is for infiltration and negative for evaporation.

454

455 5.3.2 Water balance

456 By integrating the boundary flow velocity in Fig. 13a, the total cumulative flux for the experiment and the three models were
457 obtained (**Fig 14a**). In the experiment, the variation of water flux was estimated by calculating the sum of the difference
458 between $\theta_{ini}$ (initial volume water content) and $\theta_{t=i}$ (volume water content at any time) in the five monitoring depths.
459 Meanwhile, the water evaporation during water ponding was also estimated and added to the total flux volume. Regarding
460 the numerical model, the water balance was obtained by integrating all flow components along the upper and lower boundaries.
461 The steep increase stage of each curve represents cumulative input water flux during wetting periods and the gradual decrease
462 stage represents cumulative output water flux during drying periods. To evaluate the performance of each model on the water
463 balance, the measured cumulative input and output water fluxes in each wetting and drying stage were compared to the
464 simulated ones (Fig. 14b).

465 In Fig. 14a, the results show that the total infiltration ($I_{t,inf}$) and evaporation flux ($E_{t,eva}$) estimated from measured $\theta_{exp}$ were

466 171 mm and 138.95 mm, respectively. The $I_{t,inf}$ was 5.86 % less than the supplied water (183.44 mm) due to the water leakage.

467 The $E_{t,eva}$ was 16.48 % less than the cumulative $PE$ (166.36 mm) because of the limit of the soil actual evaporation. Regarding

468 the simulation results, the coefficient of determination ($R^2$) and intercept were used to evaluate the errors made by the three

469 models. As shown in Fig. 14b, the slope of each fitting curve was fixed as 1. The SDM and DPMDy have relatively smaller

470 intercepts and slightly higher $R^2$ than that of the DPM-0.01 and DPM-0.03, indicative of a better coincidence to the measured

471 data. Overall, the errors in water balance caused by the three models were acceptable in this study.
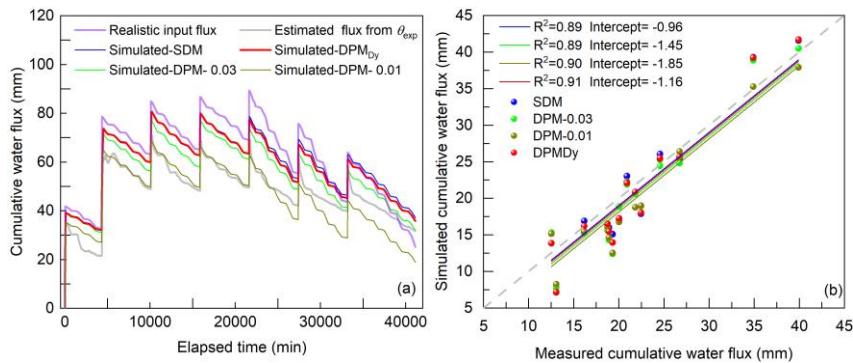
473 **Fig. 14**. Water balance for the measured and simulated results (a) Temporal evolution of total water flux calculated from the

474 measured water content, SDM, DPM and DPMDy; (b) measured versus modeled cumulative flux during each drying and

475 wetting stage

476

477 5.3.3 Crack dynamic changes and hydrological response

478 **Fig. 15** shows part of the comparison results between the measured data and the three models. Detailed descriptions of all the

479 comparison results are presented in **Appendix A**. Overall, all models show similar response trends with the measured data.

480 Divergences among the three models mainly appeared during drying.

481 In **Fig. 15a**, the simulated surficial $w_{c,sim}$ was not only generally close to the $w_{c,exp}$ in value and trend, but also it captured

482 the transient slow decrease of $w_{c,exp}$ during low evaporation periods. Notably, significant overprediction appeared in the 6$^{th}$

483 and 7$^{th}$ wetting-drying cycles.

484 In **Fig. 15b**, the matric suction ($S_{sim}$) at the 25 cm depth simulated by SDM and DPMDy was close to each other and had an

485 average divergence 2.26 kPa to the measured data. The $S_{sim}$ simulated by DPM had a greater average divergence of 3.4 kPa

486 to the measured data. They showed systematic underprediction compared to the $S_{sim}$ simulated by SDM and DPMDy, but

487 their differences became smaller with the increasing WD cycles.

488 In **Fig. 15c**, the total volumetric water content $\theta_{sim}$ simulated by SDM was much lower with respect to the DPMDy and

489 DPM. The $\theta_{sim}$ simulated by DPM-0.01 and DPM-0.03 overpredicted the volumetric water content. The DPMDy provided

490 better prediction results but also showed slight underprediction to the measured data at the last two WD cycles.
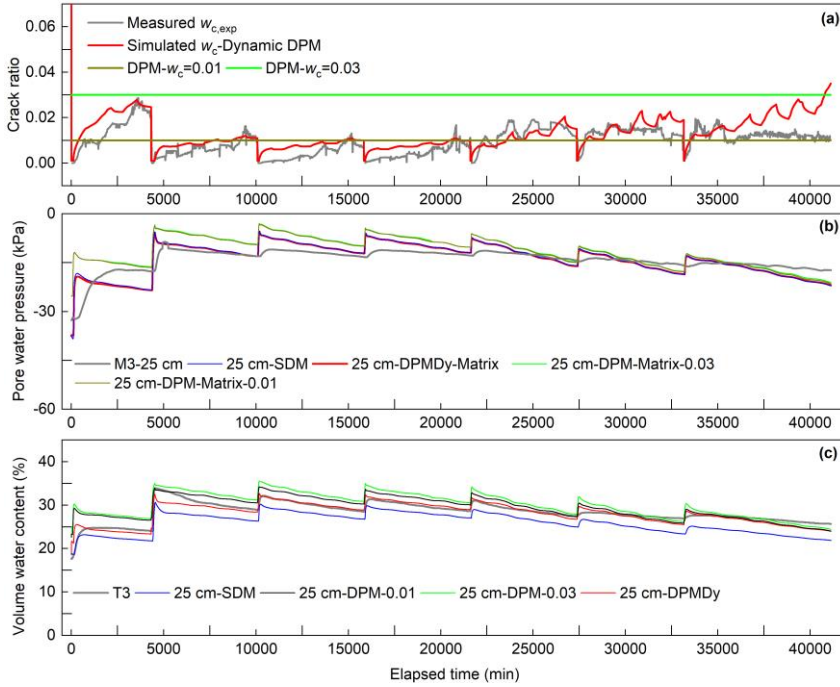
**491**
**492** **Fig. 15** Temporal evolution of the measured and simulated crack ratio, matric suction and volumetric water content. (a)
**493** Measured and simulated crack ratio on soil surface; (b) Measured and simulated matric suction at 25 cm depth; (c) Measured
**494** and simulated total water content at 25 cm depth

## 6. Discussions

6.1 Crack dynamic changes

**497** Our experimental results demonstrated that the crack evolution is not always positively correlated to the increase of the WD
**498** cycles, $T$ and $PE$. For instance, the 5 cm $\theta_{exp}$ at the end of the final three WD cycles was lower than that in the 1st WD cycle
**499** due to the increased $T$ and $PE$, but the maximum $w_{c,exp}$ measured during the final three WD cycles was much less than that
**500** in the 1st WD cycle. From the energy-driven perspective, soil cracking and propagation can be regarded as a process that the
**501** shrinkage energy (or stress), built up from the evaporation and thermal radiation, was released until a critical moment when
**502** the tensile strength of soil is reached (Peron et al., 2009; Xu et al., 2022; Tian et al., 2022). If the environmental condition
**503** changes in a stable range, the desiccation cracks will vary within the crack pattern and the maximum $w_{j,exp}$ that were formed
**504** under the maximum shrinkage energy. In this case, new desiccation cracks will not appear in the remained soil matrix during
**505** WD cycles (**Fig 5b1-b4**). One reason is that the shrinkage energy can be fully released via previous cracks. The other reason
**506** is that the shrinkage energy is not high enough to split the soil matrix that has a denser structure (or higher tensile strength)
**507** than its initial state prior to shrinkage (Luo et al., 2021). However, once the evaporation rate and thermal radiation increase
**508** to exceed the stable range, higher shrinkage energy will lead to new cracks appearing in the soil matrix that will concurrently
**509** restrain the width increase of the previous cracks (Wang et al., 2018; Xu et al., 2021). This is the reason that cracks in the
**510** final three WD cycles are finer than the first four WD cycles. Our model describes the crack evolution mainly from the
**511** hydrological-driven perspective that assumed the surface crack pattern has become stable after undergoing 13 WD cycles and
**512** has a constant function relationship with the water content. Indeed, this assumption is reasonable for natural soils under
**513** atmospheric environmental conditions. However, our experiment not only used reconstituted soil but also intensely changed

514 the environmental conditions since the 5th WD cycle. Therefore, the model overpredicted $w_{c,exp}$ at the end of the 6th and 7th

515 WD cycles.

516 In addition, another interesting phenomenon is the transient decrease of $w_{c,exp}$ and increase of $\theta_{exp}$ measured at 5 cm depth

517 during low evaporation periods, which we called as 'self-closure' process. In light of **Fig 6** and **Fig 8**, the self-closure process

518 appeared always accompanied by relatively high *RH*. From the insight of the experiment, it is natural and common to infer

519 that the moist air wetted the surface soil from top to bottom, resulting in the self-closure phenomenon. Interestingly, our model

520 does not incorporate the vapor flow into the boundary conditions, and also the evaporation boundary only involves the outflow

521 of water, but it still managed to captured the self-closure process. **Fig 16** shows the crack images at t = 3702 and 4327 min as

522 well as the corresponding cloud chart of $\theta_{sim}$. It can be seen that the soil surface became moist during the low evaporation

523 period, which is a typical external phenomenon reflecting the self-closure process. The simulation results show that $\theta_{sim}$

524 near the surface soil increased during evaporation while $\theta_{sim}$ at deep soils decreased, indicative of evaporation inducing the

525 deep water move up and wet the surface soil from bottom to top. We further found that the process occurred because the water

526 flow driven by the soil water potential gradients, existing between the wet and dry soil layers, overcame the gravity. Indeed,

527 this kind of 'hydraulic lift' process frequently occurs in planted soils where root zone soil can force water flow from moist

528 deep soil layers to dry shallow soil layers (Richards and Caldwell, 1987; Bauerle et al., 2008), but was rarely reported in

529 homogeneous bare soil. We infer that the evaporation boundary conditions using Eq. (14) might play a positive role in leading

530 water move up and constraining it within the surficial soil depths when the evaporation intensity decreased. In any case, our

531 results provide an additional possible explanation to the self-closure phenomenon. Further quantitative analysis based on gas-

532 liquid two phase flow model is needed to compare the contribution of 'hydraulic lift' and moist air to the self-closure process

533 of cracks.
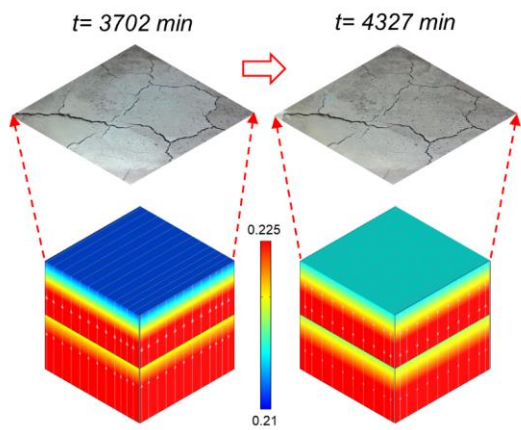
534

535 **Fig. 16** Crack images at t = 3702 and 4327 min (Photo at the top of the figures) as well as the vertical distribution of water

536 content in the numerical model (Lower part of the figures) during the low evaporation process. The left part is at the beginning

537 of the final low evaporation stage during the 1st drying periods, while the right part is at the end of the final low evaporation

538 stage during the 1st drying periods.

539

540 6.2 Water flow with dynamic changes of desiccation cracks

541 6.2.1 Water fluxes

542 As mentioned in section 5.3.1, during the drying process, the matrix and crack evaporation simulated by the DPMDy are

543 overall lower and higher than other models, respectively. It can be explained by looking at the variation of boundary $K_m$ and

$K_c$ in each model. Take the time span in **Fig.13a2** as an example, because the DPMDy considers the effects of matrix shrinkage on the $K_m$ using Eq. (26), the $K_{m,DPMDy}$ is always approximately 20% and 30% lower than that of the SDM and DPM, respectively **(Fig. 17a)**. On the contrary, because the DPM links the $K_c$ with the saturation degree of the crack domain (see Eq. (25)), the $K_{c,DPM}$ is destined to decrease with the decreased saturation degree of the crack domain induced by drying, while the $K_{c,DPMDy}$ increases with the crack development induced by drying in light of Eq. (28-b). The ultimate $K_{c,DPMDy}$ is 80% higher than the $K_{c,DPM}$ **(Fig. 17b)**. Indeed, the decrease of $K_c$ with the drying process is an unrealistic and physically-unreasonable results. We can image that after long-term drought, the $K_{c,DPM}$ will decline to nearly zero according to Fig. 12d, which will greatly underestimate the propagation of the PF-DC in the subsequent storm event. However, many laboratory and field experiments have observed that heavy rainfall following a long-term drought facilitated PF-DC (Baram et al., 2012a; 2013; Greve et al., 2010; Kurtzman and Scanlon, 2011; Schlögl et al., 2022). By contrast, the DPMDy has the potential to capture this process for its increasing $K_c$ with the enlarging desiccation crack during the long-term drought. In this study, because the experiment scale (or crack volume) is small, the increment of PF-DC simulated by the DPMDy after high-intensity evaporation is not significant (despite increment = 25%), but we believe the DPMDy will have a better performance in a larger scale (i.e slope scale).
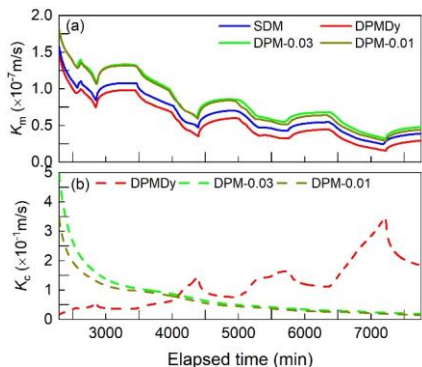
**Fig. 17** Variation of boundary $K_m$ and $K_c$ in each model during the 5th drying periods. (a) $K_m$; (b) $K_c$

6.2.2 Water exchange and distribution

For the dual-permeability model, the two domains are coupled by the water exchange term (Eq. 3) that is governed by the pressure head difference between the two domains ( $\Delta h = h_c - h_m$ ), water exchange coefficient ( $\alpha_w$ ) and the hydraulic conductivity between the two domains ( $K_a$ ). The higher the $\Gamma_w$, the quicker the two domains equilibrate. Generally, the higher $\Gamma_w$ leads to faster water exchange from the crack domain into the matrix domain and thus boosts the contribution of preferential flow on the water distribution in the soil matrix. According to the previous studies, the commonly used magnitude of the product of saturated $\alpha_w K_a$ in clay soils ranges from $10^{-5}$ m$^{-1}$s$^{-1}$ (Aguilar‐López et al., 2020) to $10^{-6}$ m$^{-1}$s$^{-1}$ (Coppola et al., 2012; 2015; Gerke and Maximilian Köhne, 2004; Vogel et al., 2000). In this study, the saturated $\alpha_w K_a$ is $1.16 \times 10^{-5}$ m$^{-1}$s$^{-1}$, which falls in the reasonable range. Building on the above statement, the $\Delta h$ and water exchange rates ( $\Gamma_w / w_m$ ) for both the DPM and DPMDy at the 5 cm, 15 cm and 25 cm depths during the 6th rainfall event are graphed in **Fig. 18**.

As shown in **Fig. 18a1-a3**, $\Delta h$ at all depths simulated by both the DPM and DPMDy rapidly reaches a positive peak value and gradually decreases with the rainfall process. The rapidly increasing positive value is because the crack domain gets

573     saturation earlier than the surrounding soil matrix due to the influx of preferential flow and the small crack storage space in

574     this study. The decrease of the $\Delta h$ is ascribed to the increase of $h_m$ with water exchanging from crack to matrix domain.

575     Notably, the crack closure process during rainfall process leads to decrease of crack volume (or crack water storage space),

576     the 'water table' (saturated zone) in the shrinking cracks elevates faster than that in the constant larger crack volume, which

577     means the $h_c$ simulated by DPMDy is higher than the DPM-0.01 and DPM-0.03. Consequently, the time for $\Delta h$ reaching

578     the peak value simulated by the DPMDy is the earliest at all the three depths, then followed by the DPM-0.01 and DPM-0.03.

579     The $\Gamma_w / w_m$ simulated by the DPMDy shows the similar trend to the $\Delta h$ **(Fig. 18b1-b3)**. During the 6th rainfall event, its

580     cumulative $\Gamma_w / w_m$ at the 5 cm, 15 cm and 25 cm depths is (26%, 50%), (10%, 26%) and (3%, 14%) larger than that of the

581     DPM-0.01 and DPM-0.03, respectively.

582     This result means that the crack closure during wetting benefits the building-up process of the pressure head in the crack

583     domain and thus can promote water exchange from crack into matrix domain. It corresponds to some experimental results

584     that the PF-DC also exists and leads water to rapidly infiltrate into soils even if desiccation cracks are nearly closed (Baram

585     et al., 2012a; Greve et al., 2010; Luo et al., 2021; Sander and Gerke, 2007; Tuong et al., 1996). It also means using DPM may

586     overestimate the flux of PF-DC, but underestimate the water exchange coming from the PF-DC. Because the experimental

587     scale, crack ratio and depth in this study is small, the difference of simulation result involving the matric suction and water

588     content between the DPM and DPMDy is not very significant. However, we can image that the deviation caused by the DPM

589     at a larger scale will be more significant, especially in a typical shrinking-swelling soil slope under long-term WD cycles.
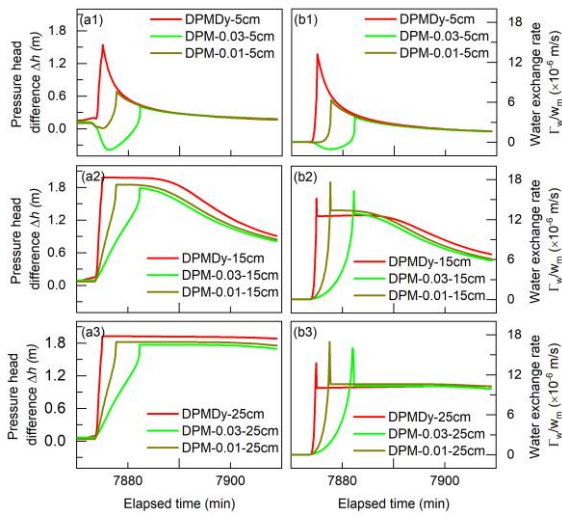
590

591   **Fig. 18** Pressure head difference (a1-a3) and water exchange rate (b1-b3) between the two domains at the 5 cm, 15 cm and

592   25 cm depths during the 6th rainfall event. The positive value of water exchange rate is for the water flowing from the crack

593   to the matrix domain, while the negative value for the opposite direction

594

595   6.3 Model performance

596   We evaluated the prediction errors of different models to the measured matric suction, water content and crack ratio using a

597   fixed slope line as the same in section 5.3.2 (see Fig. A3 and Table 4). Overall, the DPMDy, which incorporates the dynamic

598   changes of desiccation cracks and hydraulic conductivity into the dual-permeability model, has an overall better performance

599   than the SDM and DPM, as indicated by small intercept and high $R^2$. With regard to the water flux, while the three models all

600   give a good fit with the measured data, the DPM overpredicted the water flux of PF-DC but underestimated the water exchange

from cracks to soil matrix compared to other models. It implies that adopting a constant crack volume in the DPM model, whether it is an average or a maximum value of the measured crack ratio, will overestimate the PF-DC, which may be unsuitable to evaluate the irrigation efficiency. With regard to the matric suction (or pore water pressure), although the SDM has good performance as the DPMDy does, it significantly underpredicted the volume water content and thus may overestimate landslide stability in a moisture-content-dependent threshold method. Further, we expect that the SDM may show much poorer performance if one applies it to scenarios where the cracks are deeper and the soil has a higher swelling-shrinking ability than that of our experiment. A comprehensive model sensitivity analysis will be conducted in our future work.

Table 4 Summary of fitting performance of different models to measured data

| Models | SDM | | DPMDy | | | DPM-0.03 | | DPM-0.01 | |
|---|---|---|---|---|---|---|---|---|---|
| Prediction variables | $S$ | $\theta$ | $S$ | $\theta$ | $w_c$ | $S$ | $\theta$ | $S$ | $\theta$ |
| Slope | 1 | | | | | | | | |
| Confidence interval | 95% | | | | | | | | |
| Intercept | 1.51 | -1.88 | 1.35 | 0.45 | 1.02 | 3.91 | 2.19 | 3.74 | 1.79 |
| $R^2$ | 0.34 | 0.53 | 0.38 | 0.50 | 0.47 | -0.05 | 0.21 | -0.03 | 0.13 |

Compared to other dynamic preferential flow models, the DPMDy developed in this study also has its unique advantages. Firstly, the variation of crack volume (or crack ratio) in our model is deduced from the changes of matrix porosity due to shrinkage and thus has a universal definition. Instead, Coppola et al. (2012); (2015) linked the crack ratio to the suction head with an empirical natural logarithm function, which is not transferable to other types of soils. ~~Secondly,~~ Secondly, the results support the suitability, in the crack domain, where capillarity has little effect, of V-G SWRC with effective parameters and a constant relative hydraulic conductivity ($K_r$=1). In fact, a common defect in classical DPMs is that they often set the hydraulic conductivity of the crack domain ($K_c$) varies as a function of the saturated degree calculated from the SWRC of the crack domain (i.e Eq. (25)). This will lead to an unreasonable extremely low $K_c$ in drying initial conditions (Aguilar-López et al., 2020). Setting $K_r$=1 ensures that the magnitude of ~~a common defect in classical DPMs is that they often set the hydraulic conductivity of the crack domain ($K_c$) varies as a function of the saturated degree calculated from the SWRC of the crack domain (i.e Eq. (25)). This will lead to an unreasonable extremely low $K_c$ in drying initial conditions (Aguilar-López et al., 2020). In our model, we set the relative hydraulic conductivity of the crack domain to unit ($K_r$=1). It ensures that the magnitude of~~ $K_c$ only depends on the crack area or the saturated degree of the soil matrix domain, which provides a potential solution for remedying the shortcoming mentioned above. Thirdly, compared to some dynamic preferential flow models neglecting the water exchange between the two domains (Jamalinia et al., 2020; Kroes et al., 2000; Luo et al., 2021; Stewart, 2018) or that ones adopting an arithmetic mean of hydraulic conductivity of the two domains (Coppola et al., 2012; 2015; Laine-Kaulio et al., 2014; Shao et al., 2018) that tends to overestimate the water exchange, our model tentatively adopts an improved exchange term proposed by Gerke et al. (2013), which we showed to be a logical and satisfactory improvement in simulating water exchange in our experiment.

However, in the current study, the hysteresis effect was neglected in both the soil deformation and SWRC because we assumed the soil shrinking-swelling behavior has less influence on the pore-size distribution (or SWRC shape) but more influence on the porosity (or hydraulic conductivity). This assumption inevitably caused some errors when compared to the measured water content, especially for the surficial soil layer that has been significantly affected by the WD cycles. Our future work will try to incorporate the hysteresis effect into the current model to further improve the prediction strength. Besides, we have to remind again that because the shrinking-swelling model in our method is developed based on the hydrological-driven perspective, it may be more suitable in the natural soil layer where the crack pattern already has a stable state after long-term WD cycles.

## 7. Conclusions

This study combined an experimental study and a numerical simulation to quantify the preferential flow induced by dynamic changes of desiccation cracks (PF-DC). A soil column infiltration test under wetting-drying conditions was conducted to investigate dynamic changes of desiccation cracks and the accompanying water infiltration process. The variation of crack geometry, including crack ratio, width and depth were measured. The soil volumetric water content, matric suction and water drainage were also monitored. A new dynamic dual-permeability model (DPMDy) was developed to account for the PF-DC, which includes physically-consistent functions in describing the variation of both porosity and hydraulic conductivity in crack and matrix domains. The performance of the single-domain model (SDM), rigid dual-permeability model (DPM) and DPMDy was evaluated by comparing their simulation results to the monitoring data.

Overall, the DPMDy performed not only better prediction on the crack evolution and hydrological response with respect to the SDM and DPM, but also provided much better descriptions on the underlying physics involving the PF-DC. During the drying periods, the matrix evaporation modeled by the DPMDy is lower than that of the SDM and DPM due to considering the permeability decay induced by soil shrinkage. But the crack evaporation modelled in the DPMDy approach is the highest because it managed to capture the raised crack permeability induced by drying-enlarging desiccation cracks. Compared to the DPM with fixed crack volume, the DPMDy revealed that the crack closure process during wetting will lead to a faster pressure head building-up process in the crack domain and higher water exchange rates from the crack to the matrix domain. Additionally, using a fixed crack ratio in the DPM, whether it is the maximum or the average value from the experiment data, will overestimate the infiltration fluxes of PF-DC but underestimate its contribution to the matrix domain.

The DPMDy developed here has a physically-consistent definition. It remedies the shortcomings of the RDPM and other dynamic preferential flow models in defining the dynamic changes of desiccation cracks and hydraulic properties of the crack domain and interface. Future works should focus on considering the hysteresis effect of the SWRC curve during wetting-drying cycles in the model and its application to complex field situations.

## Appendix A

**Fig. A1** and **Fig. A2** show the temporal evolution of the measured and simulated crack ratio on the soil surface, matric suction (negative pore water pressure) and volumetric water contents at the five monitoring depths (5, 15, 25, 35 and 45 cm).

In **Fig A1a**, the simulated $w_{c,sim}$ was not only generally close to the $w_{c,exp}$ in value and trend, but also it captured the transient slow decrease of $w_{c,exp}$ during low evaporation periods.

In **Fig A1b-f**, the matric suction ($S_{sim}$) simulated by SDM and DPMDy is close to each other and has average divergence of 2.75 kPa, 2.26 kPa and 5.02kPa to the measured data at the 5 cm, 25 cm and 45 cm depths, respectively. The $S_{sim}$ simulated by DPM has a greater average divergence of 2.78 kPa, 3.4 kPa and 7.43 kPa to the measured data at the three corresponding depths.

In **Fig A2a-e**, the volumetric water content $\theta_{sim}$ simulated by SDM was much lower than that simulated by DPMDy and DPM. In most depths (except the 5 cm and 45 cm depth), SDM systematically underpredicted the volumetric water content during both wetting and drying periods. By contrast, the $\theta_{sim}$ simulated by DPM-0.01 and DPM-0.03 overpredicted the volumetric water content. The DPMDy gave overall better prediction results in most depths, but has significant divergences to the measured data at the depth of 5 cm and so are the other two models.
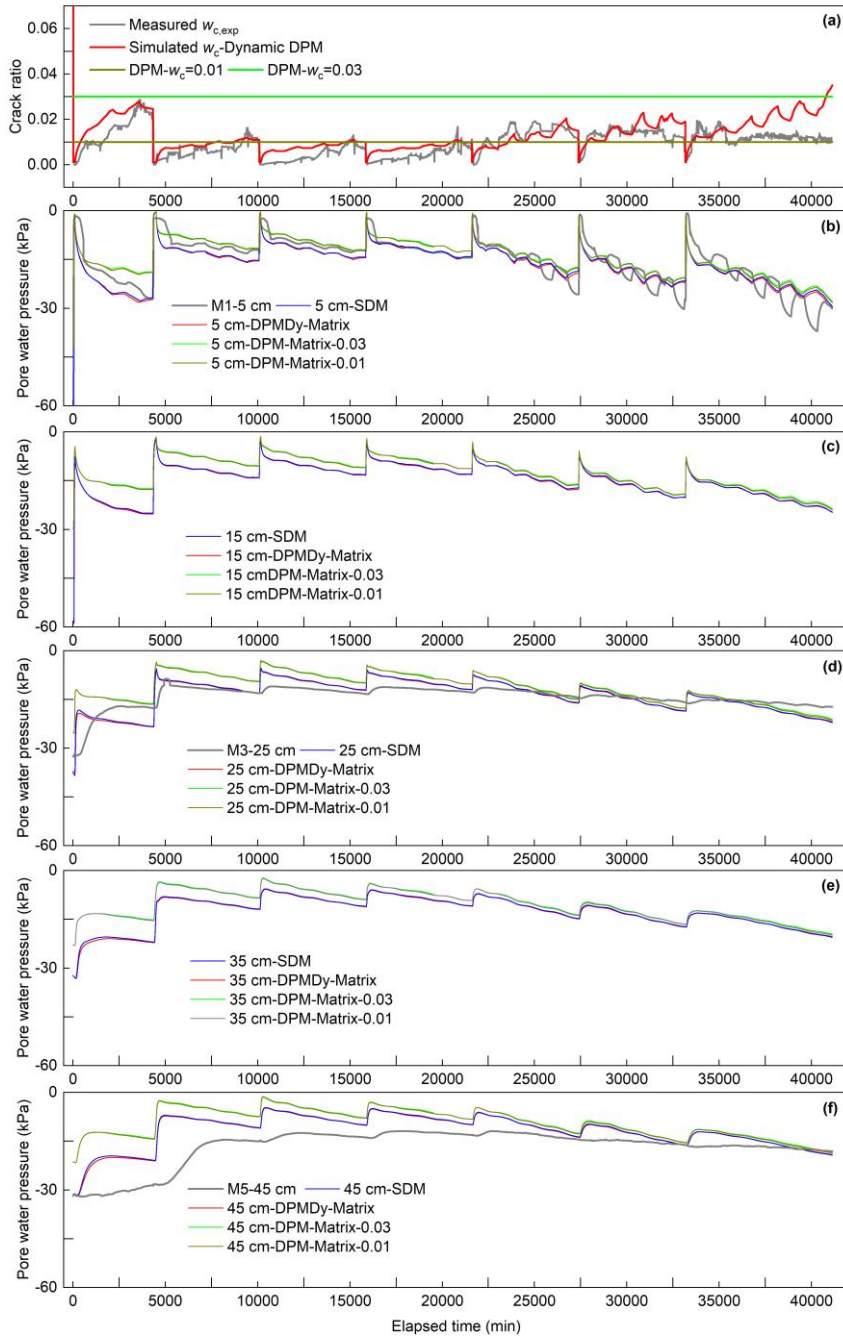
675
676 **Fig. A1** Temporal evolution of the measured and simulated crack ratio and matric suction at different depths. (a) Measured
677 and simulated crack ratio (Dynamic DPM) on soil surface; (b-f) Measured and simulated matric suction (Single domain model,
678 DPM and Dynamic DPM) at depths of 5 cm, 15 cm, 25 cm, 35 cm and 45 cm.
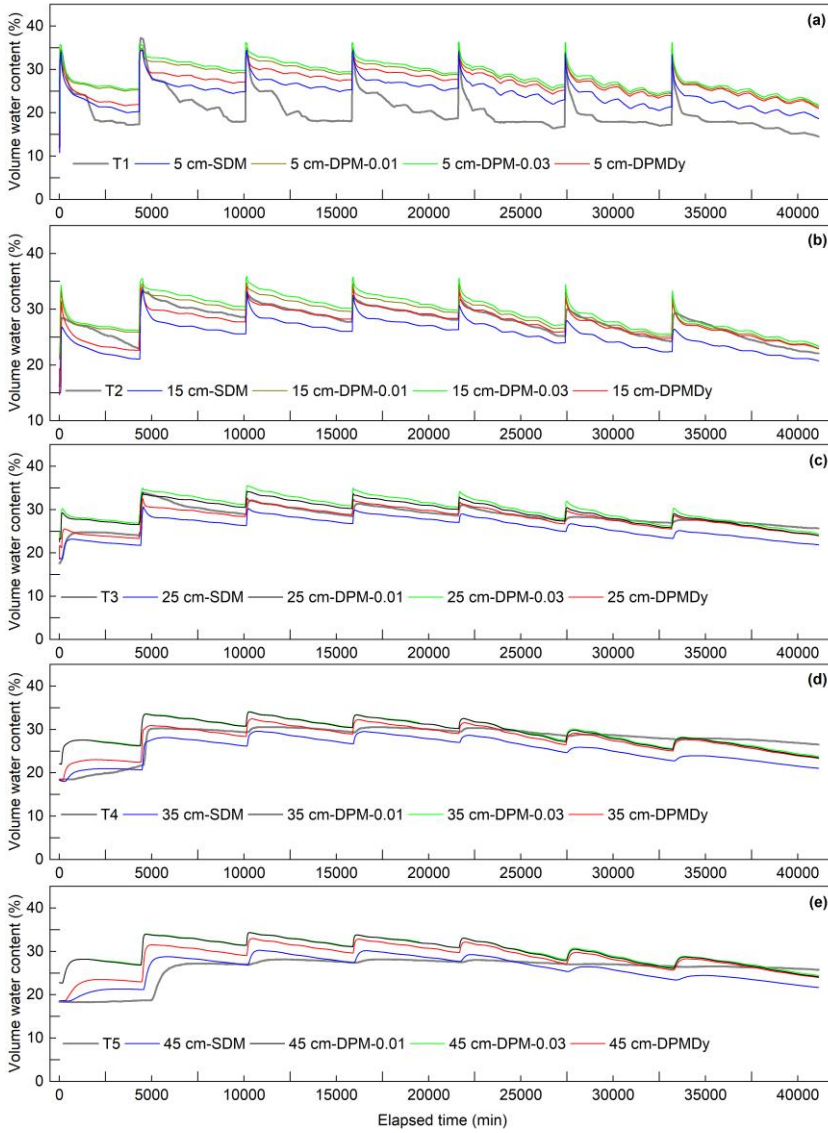
679
680    **Fig. A2** Temporal evolution of the measured and simulated volumetric water content at depths of 5 cm, 15 cm, 25 cm, 35 cm
681    and 45 cm. Note that the simulated volumetric water content demonstrated here is the total volumetric water content that
682    combined with the combined matrix and crack domains using Eq. (8)
683
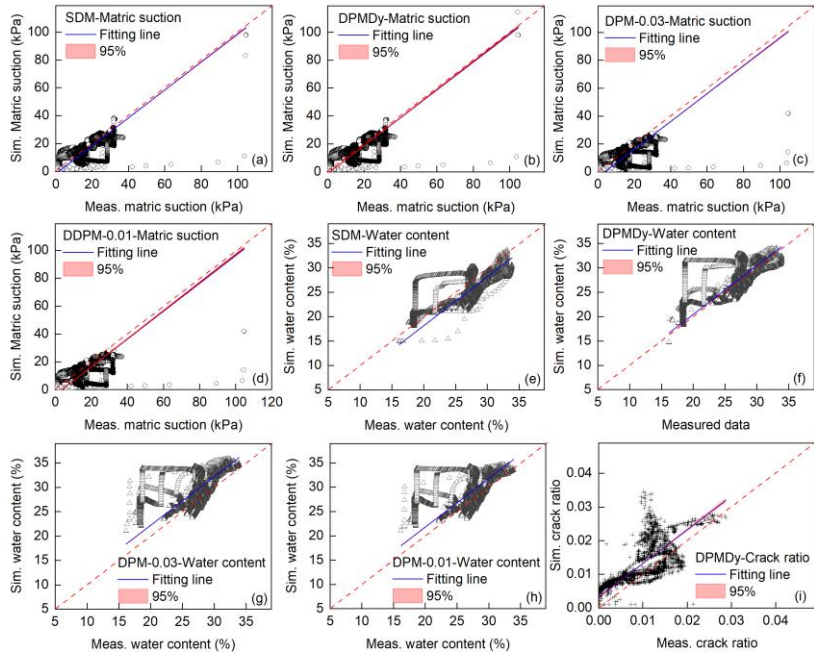
684
685 Fig A3 Scatter plots of modeled vs measured data. (a), (b), (c) and (d) refer to the matric suction simulated by SDM, DPMDy,
686 DPM-0.03 and DPM-0.01, respectively; (e), (f), (g) and (h) refer to the volumetric water content simulated by SDM, DPMDy,
687 DPM-0.03 and DPM-0.01, respectively; (i) crack ratio simulated by DPMDy. Sim. means simulated and Meas. means
688 measured.

689

690 **Notation**

| | |
|---|---|
| PF-DC | Preferential flow induced by desiccation cracks |
| SDM | Single-domain model |
| EMs | Explicit crack models |
| DPoM | Dual-porosity model |
| DPM | Rigid dual-permeability model with fixed crack ratio and hydraulic conductivity |
| DPM-0.01 | Rigid dual-permeability model with crack ratio of 0.01 |
| DPM-0.03 | Rigid dual-permeability model with crack ratio of 0.03 |
| DPMDy | Dynamic DPM with changing crack ratio and hydraulic conductivity |
| WD cycles | Wetting-drying cycles |

| | |
|---|---|
| $\theta$ | Total water content (combined matrix and crack domains), $m^3m^{-3}$ |
| $\theta_{exp}$ | Volumetric water content measured in the experiment, $m^3m^{-3}$ |
| $\theta_m$ | Volumetric water content of the matrix domain, $m^3m^{-3}$ |
| $\theta_c$ | Volumetric water content of the crack domain, $m^3m^{-3}$ |
| $\theta_{m,s}$ | Saturated volumetric water content of the matrix domain, $m^3m^{-3}$ |
| $\theta_{m,r}$ | Residual volumetric water content of the matrix domain, $m^3m^{-3}$ |
| $\theta_{c,s}$ | Saturated volumetric water content of the crack domain, $m^3m^{-3}$ |
| $\theta_{c,r}$ | Residual volumetric water content of the crack domain, $m^3m^{-3}$ |

| | |
|---|---|
| $S_{e,m}$ | Saturation degree of the matrix domain, m$^3$m$^{-3}$ |
| $S_{e,c}$ | Saturation degree of the crack domain, m$^3$m$^{-3}$ |
| $\alpha_m$ | Parameter for the van Genuchten water retention curve of the matrix domain, 1/m |
| $n_m$ | Parameter for the van Genuchten water retention curve of the matrix domain, 1/m |
| $m_m$ | Parameter for the van Genuchten water retention curve of the matrix domain, 1/m |
| $\alpha_c$ | Parameter for the van Genuchten water retention curve of the crack domain, 1/m |
| $n_c$ | Parameter for the van Genuchten water retention curve of the crack domain, 1/m |
| $m_c$ | Parameter for the van Genuchten water retention curve of the crack domain, 1/m |
| $h_m$ | Pressure head of the matrix domain, m |
| $h_c$ | Pressure head of the crack domain, m |
| $C_c$ | Specific water capacity of the crack domain which is defined as $d\theta_c / dh_c$, 1/m |
| $C_m$ | Specific water capacity of the matrix domain which is defined as $d\theta_m / dh_m$, 1/m |
| $K_s$ | Total transient saturated hydraulic conductivity of the soil (combined matrix and crack domains), m/s |
| $K_c$ | Transient hydraulic conductivity of the crack domain, m/s |
| $K_{c,s}$ | Saturated hydraulic conductivity of the crack domain, m/s |
| $K_{c,\max}$ | The maximum crack hydraulic conductivity when the crack reaches its maximum crack aperture, m/s |
| $K_{c,\min}$ | The minimum crack hydraulic conductivity when the crack reaches its minimum crack aperture, m/s |
| $K_{c,r}$ | Relative hydraulic conductivity of the crack domain, m$^3$m$^{-3}$ |
| $K_m$ | Transient hydraulic conductivity of the matrix domain, m/s |
| $K_{m,s}$ | Saturated hydraulic conductivity of the matrix domain, m/s |
| $K_{m,\max}$ | The maximum matrix hydraulic conductivity prior to soil shrinkage, m/s |
| $K_{m,r}$ | Relative hydraulic conductivity of the matrix domain, m$^3$m$^{-3}$ |
| $K_a$ | Hydraulic conductivity between the matrix and crack domains, m/s |
| $K_{a_{\min}}$ | An improved hydraulic conductivity between the matrix and crack domains reformulated by Gerke et al. (2013), m/s |
| $\Gamma_w$ | Water exchange term between the crack and matrix domains, 1/s |
| $w_c$ | Crack ratio, which is defined as volumetric ratio between the crack domain and the overall soil volume, m$^3$m$^{-3}$ |
| $w_{c,\exp}$ | Surface crack ratio measured in experiment, m$^2$m$^{-2}$ |
| $w_{j,\exp}$ | Average crack aperture (or crack width) measured in the experiment, m |
| $w_{j,\max}$ | The maximum average crack aperture measured in the experiment, m |
| $d_{\max}$ | The maximum crack depth measured in the experiment, m |
| $w_m$ | Volumetric ratio between the matrix domain and the overall soil volume, m$^3$m$^{-3}$ |
| $\alpha_w$ | Effective water transfer coefficient, 1/m$^2$ |
| $V$ | Total soil volume (combined matrix and crack domains), m$^3$ |
| $V_m$ | Volume of the soil matrix domain, m$^3$ |
| $V_c$ | Volume of the crack domain, m$^3$ |
| $V_p$ | Total pore volume, m$^3$ |
| $V_{p,m}$ | Pore volume in the matrix domain, m$^3$ |
| $V_{p,c}$ | Pore volume in the crack domain, m$^3$ |
| $\varepsilon$ | Total soil porosity (combined matrix and crack domains), which is defined as $V_p/V$, m$^3$m$^{-3}$ |
| $\varepsilon_m$ | Effective porosity of the matrix domain, which is defined as $V_{p,m}/V_m$ |
| $\varepsilon_c$ | Effective porosity of the crack domain, which is defined as $V_{p,c}/V_c$ |
| $i$ | Total effective infiltration rate (combined matrix and crack domains), m/s |
| $i_m$ | Effective infiltration rate of the matrix domain, m/s |

| | |
|---|---|
| $i_c$ | Effective infiltration rate of the crack domain, m/s |
| $e_m$ | Effective evaporation rate of the matrix domain, m/s |
| $e_c$ | Effective evaporation rate of the crack domain, m/s |
| $r$ | Rainfall intensity, m/s |
| $AE$ | Actual evaporation rate, m/s |
| $PE$ | Potential evaporation rate, m/s |
| $S$ | Total matric suction at the soil surface, kPa |
| $S_{exp}$ | Soil matric suction measured in the experiment, kPa |
| $g$ | Gravitational acceleration constant, m/s$^2$ |
| $\omega_v$ | Molecular mass of water, kg/mol |
| $\xi$ | Dimensional empirical parameter with a suggested value of 0.7 |
| $h_a$ | Relative humidity of soil overlying air |
| $\gamma_w$ | Unit mass of water, kN/m$^3$ |
| R | Universal gas constant, J/mol·K |
| $T_s$ | Soil surface temperature, ℃ |
| $\phi_{max}$ | Total porosity (or the maximum porosity) of a soil core prior to soil shrinkage, which is defined as $V_p/V$ and thus equals to the $\varepsilon$, m$^3$m$^{-3}$ |
| $\phi_{min}$ | The minimum porosity of the matrix domain, m$^3$m$^{-3}$ |
| $\phi_{matrix}$ | Porosity of the matrix domain, which is defined as $V_{p,m}/V$, m$^3$m$^{-3}$ |
| $\phi_{crack}$ | Porosity of the crack domain, which is defined as $V_{p,c}/(V_m+V_c)$, m$^3$m$^{-3}$ |
| $\phi_{sub}$ | Porosity of the subsidence zone, which is defined as voids induced by soil subsidence divided by the total soil volume, m$^3$m$^{-3}$ |
| $U$ | A unified water content, which is defined as the gravimetric water content $u$ divided by its saturated value $u_{max}$ |
| $p$ | Functional shape parameters of the soil shrinkage curve |
| $q$ | Functional shape parameters of the soil shrinkage curve |
| $v$ | Water kinematic viscosity, m$^2$/s |
| $t_p$ | Beginning of ponding time after each rainfall, min |
| $\Delta h$ | Pressure difference between the crack and matrix domains, which is defined as $h_c - h_m$ |

691

**Code/Data availability**

The source code and the data generated from this study are available from the corresponding author upon reasonable request.

**Author contribution**

Yi Luo: Conceptualization, Methodology, Investigation, Writing-original draft preparation

Jiaming Zhang*: Supervision, Writing - review & editing, Project administration

Zhi Zhou: Resources, Software, Investigation

Juan P. Aguilar-Lopez: Writing - review & editing

Roberto Greco: Writing - review & editing

Thom Bogaard: Supervision, Writing - review & editing, Funding acquisition

**Competing interests**

Some authors are members of the editorial board of journal Hydrology and Earth System Sciences. The peer-review process was guided by an independent editor, and the authors have also no other competing interests to declare.

**Financial support**

This work was financially supported by the National Natural Science Foundation of China (42177166) and the Fundamental Research Funds for National University, China University of Geosciences (Wuhan). It was also partially funded by the Plan of Anhui Province Transport Technology Progress (grant 2018030) and Engineering Research Center of Rock-Soil Drilling & Excavation and Protection, Ministry of Education (202210).

**Acknowledgment**

This paper was written during visiting research exchange of Yi Luo at TUDelft in Summer 2022. The experiment was conducted from January to March 2022 in China, Professor Ming-jian Hu and his research group are thanked for their great help in providing TDR probes. Yi Luo's Chinese colleagues Yuhao Li, Zhan Yang, Xiang Li, Zijian Shen are thanked for their contribution on the experiment monitoring. The authors also would like to thank the editor and anonymous reviewers for their valuable comments that substantially improved this paper.

720 **References**

721 Aguilar‑López, J. P., Bogaard, T. A., and Gerke, H. H.: Dual‑Permeability Model Improvements for Representation of
722 Preferential Flow in Fractured Clays, Water Resour. Res., 56, 10.1029/2020wr027304, 2020.

723 Arora, B., Mohanty, B. P., and McGuire, J. T.: Inverse estimation of parameters for multidomain flow models in soil columns with
724 different macropore densities, Water Resour Res, 47, 2010WR009451, 10.1029/2010WR009451, 2011.

725 Baram, S., Kurtzman, D., and Dahan, O.: Water percolation through a clayey vadose zone, J. Hydrol., 424-425, 165-171,
726 10.1016/j.jhydrol.2011.12.040, 2012a.

727 Baram, S., Ronen, Z., Kurtzman, D., Külls, C., and Dahan, O.: Desiccation-crack-induced salinization in deep clay sediment, Hydrol.
728 Earth Syst. Sci., 17, 1533-1545, 10.5194/hess-17-1533-2013, 2013.

729 Bauerle, T. L., Richards, J. H., Smart, D. R., and Eissenstat, D. M.: Importance of internal hydraulic redistribution for prolonging
730 the lifespan of roots in dry soil, Plant Cell Environ, 31, 177-186, 10.1111/j.1365-3040.2007.01749.x, 2008.

731 Bogaard, T. A. and Greco, R.: Landslide hydrology: from hydrology to pore pressure, WIREs Water, 3, 439-459, 10.1002/wat2.1126,
732 2015.

733 Caris, J. P. T. and Van Asch, T. W. J.: Geophysical, geotechnical and hydrological investigations of a small landslide in the French
734 Alps, Eng. Geol., 31, 249-276, 10.1016/0013-7952(1)90011-9, 1991.

735 Chaduvula, U., Viswanadham, B. V. S., and Kodikara, J.: Centrifuge model studies on desiccation cracking behaviour of fiber-
736 reinforced expansive clay, Geotext. Geomembr., 50, 480-497, 10.1016/j.geotexmem.2022.02.001, 2022.

737 Chen, C., Roseberg, R. J., and Selker, J. S.: Using microsprinkler irrigation to reduce leaching in a shrink/swell clay soil, Agric.
738 Water Manage., 54, 159-171, 10.1016/s0378-3774(01)00150-0, 2002.

739 Cheng, Q., Tang, C.-S., Xu, D., Zeng, H., and Shi, B.: Water infiltration in a cracked soil considering effect of drying-wetting cycles,
740 J. Hydrol., 593, 10.1016/j.jhydrol.2020.125640, 2021.

741 Chui, T. F. M. and Freyberg, D. L.: Implementing Hydrologic Boundary Conditions in a Multiphysics Model, J. Hydrol. Eng., 14,
742 1374-1377, 10.1061/(asce)he.1943-5584.0000113, 2009.

743 Coppola, A., Comegna, A., Dragonetti, G., Gerke, H. H., and Basile, A.: Simulated Preferential Water Flow and Solute Transport in
744 Shrinking Soils, Vadose Zone J., 14, 10.2136/vzj2015.02.0021, 2015.

745 Coppola, A., Gerke, H. H., Comegna, A., Basile, A., and Comegna, V.: Dual-permeability model for flow in shrinking soil with
746 dominant horizontal deformation, Water Resour. Res., 48, 10.1029/2011wr011376, 2012.

747 Davidson, M. R.: A Green-Ampt Model of infiltration in a cracked soil, Water Resour. Res., 20, 1685-1690,
748 10.1029/WR020i011p01685, 1984.

749 Dusek, J., Gerke, H. H., and Vogel, T.: Surface Boundary Conditions in Two-Dimensional Dual-Permeability Modeling of Tile Drain
750 Bromide Leaching, Vadose Zone J., 7, 1287-1301, 10.2136/vzj2007.0175, 2008.

751 Favre, F., Boivin, P., and Wopereis, M. C. S.: Water movement and soil swelling in a dry, cracked Vertisol, Geoderma, 78, 113-123,
752 10.1016/s0016-7061(97)00030-x, 1997.

753 Gerke, H. H. and Maximilian Köhne, J.: Dual-permeability modeling of preferential bromide leaching from a tile-drained glacial
754 till agricultural field, J. Hydrol., 289, 239-257, 10.1016/j.jhydrol.2003.11.019, 2004.

755 Gerke, H. H. and van Genuchten, M. T.: A dual-porosity model for simulating the preferential movement of water and solutes in
756 structured porous media, Water Resour. Res., 29, 305-319, 10.1029/92wr02339, 1993a.

757 Gerke, H. H. and van Genuchten, M. T.: Evaluation of a first-order water transfer term for variably saturated dual-porosity flow
758 models, Water Resour. Res., 29, 1225-1238, 10.1029/92wr02467, 1993b.

759 Gerke, H. H., Dusek, J., and Vogel, T.: Solute Mass Transfer Effects in Two-Dimensional Dual-Permeability Modeling of Bromide
760 Leaching From a Tile-Drained Field, Vadose Zone J., 12, 10.2136/vzj2012.0091, 2013.

761 Germann, P. F. and Karlen, M.: Viscous-Flow Approach to In Situ Infiltration and In Vitro Saturated Hydraulic Conductivity
762 Determination, Vadose Zone J., 15, 10.2136/vzj2015.05.0065, 2016.

763 Greco, R.: Preferential flow in macroporous swelling soil with internal catchment: model development and applications, J. Hydrol.,
764 269, 150-168, 10.1016/s0022-1694(02)00215-9, 2002.

765  Greve, A., Andersen, M. S., and Acworth, R. I.: Investigations of soil cracking and preferential flow in a weighing lysimeter filled
766  with cracking clay soil, J. Hydrol., 393, 105-113, 10.1016/j.jhydrol.2010.03.007, 2010.

767  Hendrickx., J. M. H. and Flury, M.: Conceptual Models of Flow and Transport in the Fractured Vadose Zone, in: Panel on Conceptual
768  Models of Flow and Transport in the Fractured Vadose Zone, National Academy Press, Washington D.C., 149-187, 2001.

769  Jamalinia, E., Vardon, P. J., and Steele-Dunne, S. C.: The impact of evaporation induced cracks and precipitation on temporal slope
770  stability, Comput. Geotech., 122, 10.1016/j.compgeo.2020.103506, 2020.

771  Jarvis, N., Koestel, J., and Larsbo, M.: Understanding Preferential Flow in the Vadose Zone: Recent Advances and Future Prospects,
772  Vadose Zone J., 15, 10.2136/vzj2016.09.0075, 2016.

773  Khan, M. S., Hossain, S., Ahmed, A., and Faysal, M.: Investigation of a shallow slope failure on expansive clay in Texas, Eng. Geol.,
774  219, 118-129, 10.1016/j.enggeo.2016.10.004, 2017.

775  Krisnanto, S., Rahardjo, H., Fredlund, D. G., and Leong, E. C.: Water content of soil matrix during lateral water flow through
776  cracked soil, Eng. Geol., 210, 168-179, 10.1016/j.enggeo.2016.06.012, 2016.

777  Kroes, J. G., Wesseling, J. G., and Van Dam, J. C.: Integrated  modelling  of  the  soil – water – atmosphere – plantsystem using
778  the model SWAP 2.0 an overview of theory andan  application, Hydrol. Processes, 14, 10, https://doi.org/10.1002/1099-
779  1085(20000815/30)14:11/12<1993::AID-HYP50>3.0.CO;2-%23, 2000.

780  Kurtzman, D. and Scanlon, B. R.: Groundwater Recharge through Vertisols: Irrigated Cropland vs. Natural Land, Israel, Vadose
781  Zone J., 10, 662-674, 10.2136/vzj2010.0109, 2011.

782  Laine-Kaulio, H., Backnäs, S., Karvonen, T., Koivusalo, H., and McDonnell, J. J.: Lateral subsurface stormflow and solute transport
783  in a forested hillslope: A combined measurement and modeling approach, Water Resour. Res., 50, 8159-8178,
784  10.1002/2014wr015381, 2014.

785  Larsbo, M. and Jarvis, N. J.: MACRO5.0. A model of water flow and solute transport in macroporous soil. Technical description,
786  2003.

787  Lepore, B. J., Morgan, C. L. S., Norman, J. M., and Molling, C. C.: A Mesopore and Matrix infiltration model based on soil structure,
788  Geoderma, 152, 301-313, 10.1016/j.geoderma.2009.06.016, 2009.

789  Liu, C.-W., Cheng, S.-W., Yu, W.-S., and Chen, S.-K.: Water infiltration rate in cracked paddy soil, Geoderma, 117, 169-181,
790  10.1016/s0016-7061(03)00165-4, 2003.

791  Luo, Y., Zhang, J.-m., Zhou, Z., Shen, Z.-j., Chong, L., and Victor, C.: Investigation and prediction of water infiltration process in
792  cracked soils based on a full-scale model test, Geoderma, 400, 10.1016/j.geoderma.2021.115111, 2021.

793  Mooney, S. J. and Morris, C.: A morphological approach to understanding preferential flow using image analysis with dye tracers
794  and X-ray Computed Tomography, Catena, 73, 204-211, 10.1016/j.catena.2007.09.003, 2008.

795  Mualem, Y.: A new model for predicting the hydraulic conductivity of unsaturated porous media, Water Resour. Res., 12, 513-522,
796  10.1029/WR012i003p00513, 1976.

797  Nimmo, J. R.: Theory for Source-Responsive and Free-Surface Film Modeling of Unsaturated Flow, Vadose Zone J., 9, 295-306,
798  10.2136/vzj2009.0085, 2010.

799  Nimmo, J. R., Perkins, K. S., Plampin, M. R., Walvoord, M. A., Ebel, B. A., and Mirus, B. B.: Rapid-Response Unsaturated Zone
800  Hydrology: Small-Scale Data, Small-Scale Theory, Big Problems, Front. Earth Sci., 9, 10.3389/feart.2021.613564, 2021.

801  Pei, P., Zhao, Y., Ni, P., and Mei, G.: A protective measure for expansive soil slopes based on moisture content control, Eng. Geol.,
802  269, 10.1016/j.enggeo.2020.105527, 2020.

803  Peron, H., Hueckel, T., Laloui, L., and Hu, L. B.: Fundamentals of desiccation cracking of fine-grained soils: experimental
804  characterisation and mechanisms identification, Canadian Geotechnical Journal, 46, 1177-1201, 10.1139/t09-054, 2009.

805  Richards, J. H. and Caldwell, M. M.: Hydraulic lift: Substantial nocturnal water transport between soil layers by Artemisia tridentata
806  roots, Oecologia, 73, 486-489, 10.1007/BF00379405, 1987.

807  Sander, T. and Gerke, H. H.: Preferential Flow Patterns in Paddy Fields Using a Dye Tracer, Vadose Zone J., 6, 105-115,
808  10.2136/vzj2006.0035, 2007.

809  Schlögl, J., Wimmer, B., Cramaro, L., Wirsching, J., Poll, C., Pagel, H., Kandeler, E., Huhn, C., Griebler, C., Stumpp, C., and
810  Haderlein, S. B.: Heavy rainfall following a summer drought stimulates soil redox dynamics and facilitates rapid and deep

811 translocation of glyphosate in floodplain soils, Environ Sci Process Impacts, 24, 825-838, 10.1039/d1em00527h, 2022.

812 Shao, W., Bogaard, T. A., Bakker, M., and Greco, R.: Quantification of the influence of preferential flow on slope stability using a
813 numerical modelling approach, Hydrol. Earth Syst. Sci., 19, 2197-2212, 10.5194/hess-19-2197-2015, 2015.

814 Shao, W., Yang, Z., Ni, J., Su, Y., Nie, W., and Ma, X.: Comparison of single- and dual-permeability models in simulating the
815 unsaturated hydro-mechanical behavior in a rainfall-triggered landslide, Landslides, 15, 2449-2464, 10.1007/s10346-018-1059-0,
816 2018.

817 Šimůnek, J., Jarvis, N. J., van Genuchten, M. T., and Gärdenäs, A.: Review and comparison of models for describing non-equilibrium
818 and preferential flow and transport in the vadose zone, J. Hydrol., 272, 14-35, 10.1016/s0022-1694(02)00252-4, 2003.

819 Smith, R. J., Raine, S. R., and Minkevich, J.: Irrigation application efficiency and deep drainage potential under surface irrigated
820 cotton, Agric. Water Manage., 71, 117-130, 10.1016/j.agwat.2004.07.008, 2005.

821 SNOW, D. T.: A parallel plate model of fractured permeable media, University of California, Berkeley ProQuest Dissertations
822 Publishing1965.

823 Song, L., Li, J., Garg, A., and Mei, G.: Experimental study on water exchange between crack and clay matrix, Geomech. Eng., 14,
824 9, https://doi.org/10.12989/gae.2018.14.3.283, 2018.

825 Stewart, R. D.: A Dynamic Multidomain Green-Ampt Infiltration Model, Water Resour. Res., 54, 6844-6859,
826 10.1029/2018wr023297, 2018.

827 Stewart, R. D.: A Generalized Analytical Solution for Preferential Infiltration and Wetting, Vadose Zone J., 18, 1-10,
828 10.2136/vzj2018.08.0148, 2019.

829 Stewart, R. D., Abou Najm, M. R., Rupp, D. E., and Selker, J. S.: Modeling multidomain hydraulic properties of shrink-swell soils,
830 Water Resour. Res., 52, 7911-7930, 10.1002/2016wr019336, 2016b.

831 Stewart, R. D., Rupp, D. E., Abou Najm, M. R., and Selker, J. S.: A Unified Model for Soil Shrinkage, Subsidence, and Cracking,
832 Vadose Zone J., 15, 1-15, 10.2136/vzj2015.11.0146, 2016a.

833 Tian, B.-G., Cheng, Q., Tang, C.-S., Zeng, H., Xu, J.-j., and Shi, B.: Effects of compaction state on desiccation cracking behaviour
834 of a clayey soil subjected to wetting-drying cycles, Eng. Geol., 302, 10.1016/j.enggeo.2022.106650, 2022.

835 Tichavsky, R., Ballesteros-Canovas, J. A., Silhan, K., Tolasz, R., and Stoffel, M.: Dry Spells and Extreme Precipitation are The
836 Main Trigger of Landslides in Central Europe, Sci Rep, 9, 14560, 10.1038/s41598-019-51148-2, 2019.

837 Tuong, T. P., Cabangon, R. J., and Wopereis, M. C. S.: Quantifying Flow Processes during Land Soaking of Cracked Rice Soils,
838 Soil Sci. Soc. Am. J., 60, 872-879, 10.2136/sssaj1996.03615995006000030028x, 1996.

839 van Genuchten, M. T.: A Closed-form Equation for Predicting the Hydraulic Conductivity of Unsaturated Soils, Soil Sci. Soc. Am.
840 J., 44, 892-898, 10.2136/sssaj1980.03615995004400050002x, 1980.

841 van Genuchten, M. T. and Wierenga, P. J.: Mass Transfer Studies in Sorbing Porous Media I. Analytical Solutions, Soil Sci. Soc.
842 Am. J., 40, 473-480, 10.2136/sssaj1976.03615995004000040011x, 1976.

843 Vervoort, R. W., Silburn, M., and Kirby, M.: Near surface water balance in the Northern Murray-Darling Basin, Water Sci. Technol.,
844 48, 207-214, 10.2166/wst.2003.0442, 2003.

845 Vogel, T., Gerke, H. H., Zhang, R., and Van Genuchten, M. T.: Modeling flow and transport in a two-dimensional dual-permeability
846 system with spatially variable hydraulic properties, J. Hydrol., 238, 78-89, 10.1016/s0022-1694(00)00327-9, 2000.

847 Wang, C., Zhang, Z.-y., Fan, S.-m., Mwiya, R., and Xie, M.-x.: Effects of straw incorporation on desiccation cracking patterns and
848 horizontal flow in cracked clay loam, Soil Tillage Res., 182, 130-143, 10.1016/j.still.2018.04.006, 2018.

849 Wang, Z., Liu, J., Hamoud, Y. A., Wang, Y., Qiu, R., Agathokleous, E., Hong, C., and Shaghaleh, H.: Natural (15)N abundance as
850 an indicator of nitrogen utilization efficiency in rice under alternate wetting and drying irrigation in soils with high clay contents,
851 Sci Total Environ, 838, 156528, 10.1016/j.scitotenv.2022.156528, 2022.

852 Weiler, M.: An infiltration model based on flow variability in macropores: development, sensitivity analysis and applications, J.
853 Hydrol., 310, 294-315, 10.1016/j.jhydrol.2005.01.010, 2005.

854 Wen, T., Wang, P., Shao, L., and Guo, X.: Experimental investigations of soil shrinkage characteristics and their effects on the soil
855 water characteristic curve, Eng. Geol., 284, 10.1016/j.enggeo.2021.106035, 2021.

856 Wilson, G. W., Fredlund, D. G., and Barbour, S. L.: The effect of soil suction on evaporative fluxes from soil surfaces, Canadian

857     Geotechnical Journal, 34, 145-155, 10.1139/t96-078, 1997.

858     Xie, C., Ni, P., Xu, M., Mei, G., and Zhao, Y.: Combined measure of geometry optimization and vegetation for expansive soil slopes,

859     Comput. Geotech., 123, 10.1016/j.compgeo.2020.103588, 2020.

860     Xu, J.-J., Tang, C.-S., Cheng, Q., Vahedifard, F., Liu, B., and Shi, B.: Monitoring and early detection of soil desiccation cracking

861     using distributed fibre optical sensing, Géotechnique, 1-12, 10.1680/jgeot.21.00397, 2022.

862     Xu, J.-J., Tang, C.-S., Cheng, Q., Xu, Q.-l., Inyang, H. I., Lin, Z.-Y., and Shi, B.: Investigation on desiccation cracking behavior of

863     clayey soils with a perspective of fracture mechanics: a review, J. Soils Sediments, 22, 859-888, 10.1007/s11368-021-03082-y, 2021.

864     Zhang, J., Luo, Y., Zhou, Z., Victor, C., and Duan, M.: Research on the rainfall-induced regional slope failures along the Yangtze

865     River of Anhui, China, Landslides, 18, 1801-1821, 10.1007/s10346-021-01623-7, 2021a.

866     Zhang, J., Luo, Y., Zhou, Z., Chong, L., Victor, C., and Zhang, Y.: Effects of preferential flow induced by desiccation cracks on

867     slope stability, Eng. Geol., 288, 10.1016/j.enggeo.2021.106164, 2021b.

868